공학박사 학위논문

Development of Oxydehydration Catalyst for Glycerol to Acrylic acid and Hydrogenation Catalyst of Carbon monoxide by Hetero-atom Doping Technique

이원자 도핑 기술을 이용한 아크릴산 생산용 글리세롤 산화탈수반응 촉매 및 일산화탄소 수소화 촉매 개발

2017년 2월

서울대학교 대학원

화학생물공학부

윤 양 식

Abstract

Development of Oxydehydration Catalyst for Glycerol to Acrylic acid and Hydrogenation Catalyst of Carbon monoxide by Hetero-atom Doping Technique

Yang Sik Yun

School of Chemical and Biological Engineering

The Graduate School

Seoul National University

Over the past centuries, development of efficient catalyst for the production of fuel and fine chemicals using petroleum is one of the most important works in academic and industrial fields. As the emergence of new resources replacing fossil resources, such as biomass, shale gas, etc., new catalytic systems is highly required. Among various method to develop active catalysts, doping method have attracted attention due to its effectiveness for tuning surface properties. In this thesis, by doping hetero-atom, bi-functional catalyst for the production of value-added chemicals from biomass-derived reactant was developed, and catalytic activity was controlled by manipulating electronic properties of catalysts.

Oxydehydration of glycerol is currently attracting considerable attentions. In an attempt to develop efficient catalyst for the reaction, tungsten incorporated molybdenum vanadium mixed oxide (MoVW) catalysts were designed based on computational calculations and mechanistic insights. By

incorporating tungsten into molybdenum vanadium mixed oxide (MoV) structure, the catalysts are active and selective in not only the dehydration of glycerol but also the subsequent oxidation of acrolein to acrylic acid. Structural characterization was performed by XRD, XANES, DFT calculations, Raman, and IR spectroscopies. The incorporated tungsten species enhanced the acid and redox properties of the catalyst, leading to a high selectivity to acrylic acid (30.5 %). It not only induced but also stabilized the reduced oxidation states of molybdenum and vanadium atoms, as confirmed by XPS and DFT calculations. Hence, a stable and selective production of acrylic acid was achieved with full glycerol conversion for 110 h. The MoVW catalytic system with an additional acid catalyst bed exhibited remarkable selectivity for acrylic acid (47.2 %), suggesting its potential for practical applications.

In the fundamental aspect, catalytic activity in heterogeneous catalysis was controlled by tuning electronic state of a catalyst by doping method. For controlling the electronic state of metal supported graphene catalysts, type (N and B) and concentrations of dopants was varied. The change in electronic state of active metals was confirmed by XPS analysis. Although factors affecting on activity, such as particle size, phase, loading amount, were excluded among the prepared catalysts, different catalytic activities were observed. Theoretical calculations revealed that variation in interactions between active metal and reactant, induced by tuning the electronic state, affected catalytic activity of the catalysts.

Keywords: Heterogeneous catalyst, doping, oxydehydration, glycerol, acrylic acid, electronic state, graphene, hydrogenation.
Student Number: 2011-21052

Contents

List of Tables

List of Figures

Chapter 1. Introduction

1.1 Heterogeneous catalysis by doped catalysts

Heterogeneous catalysts constitutes a key technology for the production of fuel and fine chemicals from fossil resources [1,2]. As the need and the amount of usage for chemicals were increased, it is clear that our reliance on fossil resources have been grown, leading to depletion of fossil fuel [3-7]. In addition, the economic and environmental impacts have drastically emerged. Thus, there is a push towards reducing the usage of fossil resources, and the utilization of alternative resources, such as biomass, shale gas, etc. This calls for the development of new and improved catalytic system with efficiency.

For the development of alternative process using renewable resource to conventional process, efficient catalysts has to be designed. Researchers tried to develop and optimize catalystic system to enhance catalytic performance in specific reactions (Figure 1-1). For example, metal-support interaction, dispersion of active site, oxidation state of catalyst, additive etc. were studied in a range from macro to nano-scale [8-10]. Among them, doping technique has attracted attention as a facile and important method for giving new chemical properties [11]. Numerous works of doping in metal oxide and carbon have been studied in the heterogeneous catalysis, photo-catalysis, electrochemistry, and sensing [11-13]. It was reported that even a small fraction of dopant in a host material can modify chemical bonding at the

surface of the host, and surface feature (eg. acid and redox properties) [11]. The change could affect adsorption and desorption behaviors on the surface, leading to modification of catalytic performance. Therefore, it was recognized that the use of doping technique is appropriate to develop catalysts efficiently.

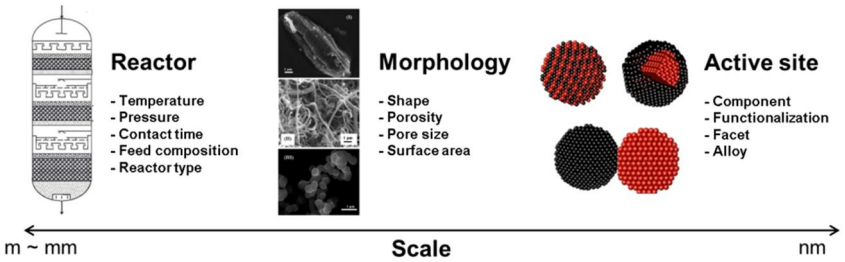

Figure 1-1. Optimization of catalytic system from reactor to atomic scales.

1.2 Design of bi-functional catalyst for glycerol oxydehydration to acrylic acid

The oxydehydration of glycerol represents an alternative route to the petrochemical-based commercial process for the acrylic acid production. Acrylic acid is widely used as base material for paints, plastics, superabsorber polymers, and rubber synthesis [14-16]. The growing demand for plastics and superabsorbers in the polymer industry has stimulated intense interest in the sustainable production of acrylic acid [16]. The alternative reaction involves the sequential dehydration of glycerol to acrolein, followed by the selective oxidation of acrolein to acrylic acid [14]. This process faces several issues. For instance, multiple steps, which can lead to additional cost and work up, and waste generation, are involved [17,18]. Due to the high toxicity, volatility, and the reactivity of intermediates, especially acrolein, the handling of intermediates is difficult, and further isolation is required [19]. For the purpose of eliminating these limitations, therefore, the development of integrated process using a bi-functional catalyst for the direct conversion of glycerol to acrylic acid is highly desirable.

1.3 Control of catalytic reactivity by tuning electronic state via doping method

The maximizing of catalytic activity is of importance for energy-efficient process in the chemical industry [20-22]. In heterogeneous catalysis, various approaches have been applied to augment the reactivity of a catalyst. For example, factors related to reaction conditions such as temperature, contact time, etc. have been optimized for achieving the desired catalytic performance [23]. In a range from the macro- to nano-scale, structure, surface area, pore size, and structure of a catalyst have been controlled [24-26]. Surface atomic coordination and composition were considered at atomic-level [27].

Recently, the advances in characterization tools and theoretical calculations allow fundamental understanding for catalysis. It has been revealed that electronic structure of a catalyst has influence on its catalytic reactivity. Core-shell, alloy, size control, lattice mismatch, and so on have been used as strategies for achieving the variation in electronic structure of a catalyst [28-31]. However, the approaches change not only the electronic structure of a catalyst but also other parameters determining catalytic reactivity such as composition, shape of a catalyst. In addition, for most of approaches to obtain the variation in electronic structure, preparation step of a catalyst is so complicated, and required high-quality techniques (ex. atomic layer deposition etc.). Although electronic structure is effective to influence

catalytic reactivity, there is lack of facile strategies to manipulate the electronic structure of a catalyst.

1.4. Objectives

The objectives of this thesis are designing bi-functional catalyst for oxydehydration of glycerol to acrylic acid by doping method, and controlling catalytic activity by tuning electronic state of catalyst by doping hetero-atom into carbon support.

In following section, Chapter 2, bi-functional catalyst for the direct conversion of glycerol to acrylic acid is developed. To achieve this, both of acid and redox properties are required. Enhancements of the properties were derived by incorporation of hetero-atom.

Finally, control of catalytic activity by tuning electronic state of catalysts was discussed. The variation of electronic state of catalysts was induced by chemical doping of graphene. Kinetic and theoretical study is included to reveal the effect of electronic state on catalytic activity.

Chapter 2. Development of a bi-functional catalyst for oxydehydration of glycerol to acrylic acid

2.1 Introduction

The oxydehydration of glycerol gives an alternative route to the petrochemical-based commercial process (oxidation of propylene oxide) for the acrylic acid production. A bi-functional catalyst for the direct conversion of glycerol to acrylic acid generally requires a combination of acid and selective oxidation properties without degradation of each active structure. However, the active structure (molybdenum vanadium mixed oxide) for the selective oxidation of acrolein is metastable, and it is easily influenced by pH and the metal concentration of the solution, the type of precursor, the activation process, etc [16,32,33]. Accordingly, a combination of two features with maintaining each intrinsic function is a significant challenge. In addition to a combination of two functions in one catalyst, it should possess suitable properties for each reaction. The first step, the dehydration reaction, proceeds in the presence of weak-to-medium acid strength acid sites [34]. For the selective oxidation of acrolein, the Mars-van Krevelen mechanism is widely accepted [35]. Based on this mechanism, unsaturated atoms with a high electron density and electronegativity act as adsorption sites for acrolein

with an allylic intermediate being formed [36,37]. A nucleophilic and weakly bonded lattice oxygen on the catalyst surface is necessary for C-H activation and the selective insertion of oxygen into the intermediate [38,39]. In addition, it has been reported that vanadium as a redox center showing V^{4+} favors the selective oxidation of acrolein by stabilizing the oxygenated species in the form of acrylate [37,40].

Despite importance and necessity of bi-functional catalyst for oxydehydration of glycerol, only a few catalysts have been developed for the direct conversion of glycerol to acrylic acid owing to above complexity of requirements for bi-functional catalyst [41-46]. Although some of the catalysts have been somewhat successful from the standpoint of performance, there has been scant discussion on fundamental understanding about active properties of catalysts and their relations to catalytic activity. As a result, time- and labor-consuming "trial-and-error" processes would be involved again in the development of new catalysts with better performance [47].

Density functional theory (DFT) can be used to provide information regarding the mechanism of heterogeneous catalysis and the intrinsic properties of materials [48-50]. In addition, advancements made in computational power and accuracy now provide a platform for catalyst design based on extensive computational screening [51]. Several studies have achieved success in catalyst design at the atomic level through model prediction by DFT calculations and experimental demonstration [52-54]. Taking this into account, a combination of innovative computational

calculations with accumulated knowledge can permit a catalyst with a high performance to be designed efficiently.

Herein, tungsten incorporated molybdenum vanadium mixed oxide (MoVW) catalysts as effective bi-functional catalysts for the direct conversion of glycerol to acrylic acid are reported. Tungsten can be a good candidate as an acidic material to be combined with molybdenum vanadium mixed oxide (MoV) because it can work as a structure promoter [16,34,55]. The concept of incorporating an acidic tungsten species into the molybdenum vanadium mixed oxide framework allows the catalyst to be active and selective for both the dehydration of glycerol to acrolein and the subsequent oxidation of acrolein to acrylic acid. We initially employed DFT calculations to investigated effect of tungsten on the electron density of neighboring atoms. The calculations were then confirmed by experiments. Finally, activity and stability tests were tested in single bed and two bed systems to confirm the enhanced catalytic behavior of the MoVW catalysts compared to MoV catalyst for the oxydehydration of glycerol. These comprehensive experiments, accompanied by DFT calculations revealed the origin of enhanced catalytic performance of the catalyst. To the best of our knowledge, this is the first report of the use of a combination of experimental and theoretical studies for developing an efficient catalyst in this research area.

2.2 Experimental

2.2.1 Preparation catalysts

Ammonium molybdate hydrate (99.0%, Samchun), vanadium oxide sulfate hydrate (97.0%, Sigma-Aldrich), ammonium metatungstate hydrate (99.0%, Sigma-Aldrich) were utilized as the metal precursor. Oxalic acid (98.0%) was purchased from Aldrich. All precursors were used without further purification.

MoVW samples were prepared by a hydrothermal method. 7.06 g (40 mmol) of ammonium molybdate hydrate and 2.54-22.85 g (10-90 mmol) of ammonium metatungstate were dissolved in deionized water (96 mL). A stirred solution including 2.53 g (10 mmol) of vanadium oxide sulfate hydrate and deionized water (96 mL) was added to prepared solution. The mixture was stirred for an additional 10 min, and its pH value was then adjusted to 2.2 with 9 vol.% aqueous sulfuric acid solution. The resulting solution was loaded into a glass-lined autoclave (real volume: 240 mL), and heated at 175 ^{o}C for 48 h. The solid product was separated from the solution by filtration, washed with deionized water, and dried at 80 ^{o}C overnight. The prepared samples heat-treated in N_2 stream (50mL/min) at 500 ^{o}C for 2 h. The final catalysts are referred to as MoVW-X where X indicates molar ratio of tungsten compared to vanadium in preparation solution.

Reference samples, molybdenum vanadium mixed oxide (MoV) and tungsten oxide (WO_3), were also prepared according to previous reports [43,56]. In a typical experiment, 7.06 g of ammonium molybdate hydrate

dissolved in 96 mL of deionized water was mixed with 2.53 g of vanadium oxide sulfate hydrate dissolved in 96 mL of deionized water. The mixture was stirred for 10 min, followed by adjustment of pH value to 2.2 with aqueous sulfuric acid solution (9 vol.%). The resulting solution was transferred to a glass-lined autoclave, and heated at 175 ^{o}C for 20 h. In case of WO_3, aqueous solution of ammonium metatungstate hydrate with oxalic acid (molar ratio of oxalic acid to W = 3) was located in a glass-lined autoclave, and heated at 175 ^{o}C for 48 h. Both samples were recovered by filtration, washed with deionized water, dried at 80 ^{o}C overnight. The dried powdery samples of MoV and WO_3 were calcined in a stream of N_2 at 400 ^{o}C for 4 h and at 600 ^{o}C for 2 h respectively.

2.2.2 Characterization

Ultraviolet-visible (UV-Vis) spectra were recorded with a Jasco V670 spectrometer. The measurements were performed at 200-1000 nm in ambient atmosphere with 200 times diluted samples. XRD patterns of the catalysts were measured by using a Rigaku d-MAX2500-PC powder X-ray diffractometer operating at 50 kV and 100 mA using CuKa radiation (1.5406 Å). High-resolution transmission electron micrograph (HR-TEM) images were obtained on JEOL JEM-3010 microscope with an acceleration voltage of 300 kV. High angle annular dark field scanning transmission microscopy (HAADF-STEM) image and corresponding elemental mapping images were acquired by means of FEI Tecnai F20 instrument equipped with an X-ray

energy dispersive spectrometer. The specific surface areas of the samples were determined by N_2 adsorption at -196 ^{o}C, using the multipoint BET analysis method, with a Micromeritics ASAP-2010 system. The elemental compositions of the samples were determined by electron probe microanalysis (EPMA) using a JEOL JXA-8900R spectrometer. FT-IR spectra were obtained on a Nicolet 6700 (Thermo Scientific) FT-IR spectrophotometer in the range of 500-1100 cm^{-1}. The powdery samples were mixed with KBr (0.6 wt.%) and pressed into translucent disks at room temperature. Raman spectroscopy was performed on a HORIBA Jobin Yven US/HR-800 using a multichannel charge-coupled device (CCD) detector at room temperature. The external laser source was used for excitation, a He-Ne laser at 632.8 nm. X-ray absorption spectroscopy (XAS) was carried out in transmission mode at the 8C nano XAFS beamline of Pohang Light Source (PLS) in the 3.0 GeV storage ring, with a ring current of 70-100 mA. A Si (111) double-crystal was used to monochromatize the X-ray photon energy. Ionic chambers filled with N_2 (95%)/Ar (5%) and Ar (100%) were used for the I_0 and I detectors, respectively, at the W L_1-edge region. The samples were located between the ion chambers. Energy calibration of the W L_1-edge was carried out using Au foil. X-ray absorption near edge structure (XANES) spectra were recorded for each sample at room temperature using an energy step of 0.2 eV. The obtained data were normalized by Athena software [57].

The NH_3 temperature-programmed desorption (NH_3-TPD) profiles were measured on a Micromeritics Autochem II chemisorption analyzer. A 0.1 g

of sample loaded in a U-shaped quartz reactor was pretreated in a He flow (50 mL/min) at 200 ^{o}C for 1 h, and then cooled to room temperature. The samples were then exposed to a NH_3 gas mixture (10. 3% NH_3/He, 50 mL/min) and kept at 50 ^{o}C for 1 h for adsorption. The NH_3 that was physisorbed to the sample was eliminated by a flow of He (50 mL/min) at 100 ^{o}C for 30 min. NH_3-TPD profiles were obtained in a He flow (50 mL/min) by heating up to 500 ^{o}C at a rate of 10 ^{o}C/min. The desorbed NH_3 was measured by means of a thermal conductivity detector (TCD). X-ray photoelectron spectroscopy (XPS) was performed with a Sigma Probe instrument (ThermoVG). The binding energy of each element was calibrated by using the carbon peak as standard (C 1s = 284.5 eV). Peak assignment for each oxidation state of elements was conducted referring to previous researches [58-61]. The reducibility of the catalysts was studied by H_2 temperature-programmed reduction (H_2-TPR) experiments performed in a gas flow system measured by means of an online mass spectrometer (QGA, Hiden Analytical). The catalyst sample (50 mg) was placed in a U-shaped quartz reactor and pretreated in flowing Ar at 200 ^{o}C for 2 h, followed by cooling at room temperature. The temperature was then raised from room temperature to 700 ^{o}C with a heating rate of 10 ^{o}C/min in a 10% H_2/Ar flow (50 mL/min). The main (m/z) fragments registered were H_2 = 2, and Ar = 40.

2.2.3 Catalytic activity test

The catalytic activity tests were carried out at atmospheric pressure in the temperature range from 250 ^{o}C to 350 ^{o}C. A 0.3 g of powder sample was loaded into a quartz reactor (8 mm inner diameter), the reactor was then placed in an electric furnace. The temperature of the catalyst bed was monitored by a thermocouple and controlled through a PID controller.

Before the reaction, the catalyst was preheated to the reaction temperature under an inert (He and N_2) flow (27.5 and 2.93 mL/min) for 1 h. A 1.2 M aqueous solution of glycerol was vaporized at a rate of 2 mL/hr using a syringe pump. The vaporized reactant solution was diluted with a mixture of He, N_2, O_2 flow at the vaporizer, and then fed into the catalyst bed. The molar composition of the reaction mixture used was [Glycerol/O_2/H_2O/N_2/He]=[1.3/2.6/55.1/37.0/3.9]. The reaction products were passed through a condenser, and then collected in a cold trap that contained 20 mL of water and 1 mL of a 2 M 1-propanol aqueous solution. The collected products were analyzed by a gas chromatograph (Younglin ACME 6500 model) equipped with a FID detector and a HP-Innowax capillary column. 1-propanol was used as internal standard for analyzing the liquid-phase products. The gaseous products were analyzed by an online GC (Younglin ACME 6000 model) equipped with a TCD detector and a Supelco Carboxen 1000 column. N_2 was used as internal standard for analyzing the gas-phase products. Glycerol conversion and product selectivity were calculated as follows:

$$\text{Glycerol conversion (\%)} = \frac{\text{mole of glycerol reacted}}{\text{mole of glycerol fed}} \times 100$$

$$\text{Yield (\%)} = \frac{\text{mole of product}}{\text{mole of glycerol fed}} \times \frac{C_i}{3} \times 100$$

$$\text{Selectivitiy}\ (\%) = \frac{\text{mole of product}}{\text{mole of glycerol reacted}} \times \frac{C_i}{3} \times 100$$

where C_i represents the number of carbon atoms of i product.

Carbon balance was calculated by summing up the unreacted glycerol and the total amount of detected products. Carbon balances were below 100% in each run because minor and heavy products with uncertain quantity were included, some product might be decomposed during analysis in chromatograms, and some volatile product might be missed in condensing part.

2.2.4 Computational details

The Vienna Ab-initio Simulation Package (VASP) was used for density functional theory (DFT) calculations [62]. We employed the generalized gradient approximation (GGA) parameterized by the Perdew-Burke-Ernzerhof (PBE) exchange-correlation functional [63]. Ionic cores were described by the projector augmented wave (PAW) method [64]. The wave functions were constructed from the expansion of planewaves with an energy cutoff of 520 eV. A 1×1×4 Monkhorst-Pack k-point mesh was used to sample the Brillioun zone. The self-consistent iterations were converged within a criterion of 4×10^{-4} eV, and the ionic optimization steps were converged to 0.03 eV/Å. Atomic charge analysis was performed using a Bader charge analysis [65].

Equation (1) and (2) are our definitions of the substitutional (ES) and interstitial incorporation energy (EI) of tungsten atom respectively:

$$E_S = (E_{W\ sub\text{-}MoV} + E_{Mo\ or\ V}) - (E_{MoV} + E_W) \quad (1)$$

$$E_I = (E_{W\ inter\text{-}MoV}) - (E_{MoV} + E_W) \quad (2)$$

where $E_{W\ sub\text{-}MoV}$ is bulk energy of MoV unit cell in which tungsten atom is substituted for molybdenum or vanadium atom, $E_{W\ inter\text{-}MoV}$ is bulk energy of MoV unit cell in which tungsten atom is interstitially inserted into the MoV structure, $E_{Mo,\ V,\ or\ W}$ is the bulk energy of the corresponding metal per atom, and E_{MoV} is the bulk energy of MoV unit cell. More negative value of E_S and E_I means that the system is in the more stable state.

In order to evaluate the charge transfer by introducing tungsten, charge difference density was calculated using Equation (3) [66,67].

$$\Delta\rho = \rho_{MoVW} - (\rho_{MoV} + \rho_W) \quad (3)$$

where ρ_{MoVW} is the total charge density of the MoVW system, ρ_{MoV} and ρ_W are the charge density of the system without tungsten and the isolated tungsten atoms, which are placed at the same atomic position as in the MoVW system. From the equation, variations in charge induced by interaction between host and foreign systems can be obtained by subtracting non-interaction systems from interaction system.

2.3 Results and discussion

2.3.1 Modeling of tungsten incorporated MoV catalyst by DFT

Incorporating tungsten species into the MoV structure would facilitate dehydration of glycerol because tungsten oxide is well-known as an effective acid catalyst. However, it is hard to expect the effect of the presence of tungsten on selective oxidation reaction before preparation and characterization of catalysts. Therefore, we introduced DFT calculations to confirm whether the desired properties for selective oxidation of acrolein to acrylic acid are derived by incorporating acidic tungsten species into MoV structure.

To develop tungsten in6corporated molybdenum vanadium mixed oxide (MoVW) structure for DFT calculations, we attempted to identify the position of incorporated tungsten species in the MoV structure. To accomplish this, orthogonal MoV structure was first developed and optimized (Figure 2-1). We then calculated incorporation energies of tungsten into various positions in the MoV structure. The positions were chosen by considering the manner of incorporation (substitutional or interstitial incorporation) and the periodic nature of DFT calculations (Figure 2-1). Table 2-1 shows the DFT results for the substitutional (E_S) and interstitial (E_I) insertion energy of a tungsten atom at various positions calculated using Equation (1) and (2). The ES values were lower than E_I values, indicating that the substitutional incorporation of tungsten was more favorable than the interstitial incorporation of tungsten. In terms of the type

of the substituted atom, the tungsten atom was thought to substitute in preference to the molybdenum atom rather than the vanadium atom. Based on the results of energy and probability calculations (Table 2-1~2-4), we developed MoVW models (Figure 2-2), and possible configurations for each model were also listed in Table 2-5~2-8. Details for modeling MoVW were discussed in Supporting Information.

Figure 2-3 and Figure 2-4 shows charge transfer induced by introducing tungsten. The electrons were confirmed to transfer from a substituted tungsten atom to the surrounding oxygen, molybdenum, and vanadium atoms. Clearly, oxidation states of molybdenum and vanadium atoms were reduced and lattice oxygen atoms around tungsten atoms became more nucleophilic due to a gain of electrons. Therefore, it was confirmed that by incorporating tungsten into MoV framework, the properties which are required for selective production of acrylic acid, such as abundant of reduced state of molybdenum and vanadium atoms and nucleophilic oxygen, were induced [39,68].

Using Bader charge analysis, variation of oxidation state with different tungsten fraction was examined (Table 2-9). It was observed tungsten atoms were present in a high oxidation state compared to molybdenum and vanadium atoms. The oxidation state of molybdenum and vanadium atoms was decreased as increase of tungsten contents. This clearly demonstrates that tungsten induced reduced state of redox center (vanadium) and molybdenum [69]. From this, it is expected that the catalysts with high tungsten content would exhibit high performance in acrylic acid production

due to the most reduced oxidation state of vanadium among the catalysts. Consequently, by comprehensive DFT calculation, we confirmed the incorporated tungsten change intrinsic properties, which can lead to high selectivity to acrylic acid.

2.3.2 Structural characterization

MoVW catalysts were verified as good candidate with high selectivity for acrylic acid production by using DFT calculations. Hence, we intended to develop real catalysts, which have similar structure with theoretical models, for testifying to the results experimentally. The catalysts with tungsten containing MoV structure were prepared by means of a hydrothermal reaction. In the synthetic mechanism via hydrothermal reaction, a pentagonal $(M)M_5O_{21}$ polyoxometalate unit (building block) is essential for formation of the molybdenum vanadium mixed oxide structure. UV-vis spectra were collected to confirm whether the building block is formed in the preparation solution even with the tungsten precursor (Figure 2-5). All of the spectra of the MoV and MoVW solutions showed a peak at around 510-550 nm, similar to that of $Mo_{72}V_{30}$ which consists of pentagonal polyoxomolybdate units connected with vanadium centered octahedrons [33,70] From this results, the presence of the building block in the MoVW precursor solution even in the presence of a large amount of tungsten precursor is confirmed.

X-ray diffraction (XRD) was employed to investigate the crystalline structure of the MoV and MoVW catalysts, and the corresponding results are

shown in Figure 2-6A. The MoV and MoVW catalysts (except for the MoVW-9 catalyst) exhibited the characteristic diffraction of amorphous molybdenum vanadium mixed oxide (amorphous MoV) structure without any evidence for the presence of WO_x phase even in high levels of tungsten (MoVW-7) [71]. Therefore, it was confirmed that molybdenum vanadium mixed oxide structure containing tungsten species was successfully developed. The XRD patterns showed highly intense peaks at $2\theta = 22^o$ and 45^o, and broad peaks at ca. $2\theta = 10^o$ and 26^o, corresponding to layered structures with disordered slabs and an ordered layer distance along the [001] direction (c-direction), respectively [71,72]. Previous papers have reported that the unique structure are essential for the selective oxidation of acrolein to acrylic acid [73]. Accordingly, the catalysts are expected to be active and selective for the conversion of acrolein to acrylic acid.

The crystalline peak ($2\theta = 22^o$) was shifted to a higher angle with increasing tungsten content, while the structure was maintained (Figure 2-6B). This is clear evidence for incorporation of tungsten into the framework. Table 2-10 shows the theoretically and experimentally calculated lattice parameters along the c-direction. The both parameters showed a similar trend along tungsten fractions. This result clearly demonstrates as-prepared MoVW catalysts are well-synthesized as we designed by DFT-designed models.

Unlike the trends for the crystalline peaks, the peaks around $2\theta = 10^o$ and 26^o became broader with increasing tungsten content, indicating that slab plane became more disordered. When the ratio of tungsten to vanadium reached 9, the catalyst no longer showed the unique structure of amorphous

MoV, but, rather, exhibited characteristic peaks corresponding to hexagonal tungsten bronze [43]. The reason for this, we suggest, is that the hexagonal tungsten bronze structure becomes thermodynamically more stable than the amorphous MoV structure in the preparation process as degree of irregularity of the a-b plane increases in the presence of a high content of tungsten.

The TEM images of MoVW showed that the samples are rod-shape with an average diameter in range of 20-40 nm as shown in inset of Figure 2-7. Magnified HR-TEM images confirmed that the MoVW-1 to 7 samples have a layered-type structure along the c-direction without other lattices such as WO_3 (Figure 2-8). This unique structure is analogous to the structure of crystalline MoV [56], suggesting that the structure of MoV was maintained even in the presence of tungsten. While exhibiting an ordered array along the c-direction, the lattice oriented parallel to the c axis appeared to show irregularity. These results suggest that the MoVW samples had a disordered a-b plane and a highly ordered layer distance of about 4Å along the c-direction, which is consistent with the XRD results (Figure 2-6).

In order to examine the homogeneity of tungsten, high angle annular dark field (HAADF) images and corresponding elemental mapping images of MoVW-1 and MoVW-5 were obtained (Figure 2-9). Molybdenum, vanadium, and tungsten atoms were homogeneously dispersed throughout the MoVW-1 and MoVW-5 catalysts. This clearly indicates that no phase separation occurred, regardless of the magnitude of the tungsten fraction in the samples.

To further investigate the structure of MoVW catalysts, FT-IR and Raman

analyses were conducted (Figure 2-10). In the case of MoV catalyst, peaks at 915 cm^{-1} for V=O, 870 cm^{-1} for Mo=O, 652, 716, and 917 cm^{-1} for Mo-O-Mo and 604 cm^{-1} for Mo-O-V were obtained in FT-IR spectrum (Figure 2-10A). Similarly, sharp bands at 285, 819, 871 and 997 cm^{-1} attributed to Mo-O-Mo and Mo=O respectively, were observed in Raman spectra (Figure 2-10B). These are in agreement with the characteristic peaks corresponding to a molybdenum vanadium mixed oxide [68,71]. However, a change was noted in the case of the tungsten-containing catalyst. Despite the small proportion of tungsten in the MoVW-1 catalyst (EPMA results in Table 2-11), the bands attributed to Mo=O and Mo-O-Mo were decreased considerably. Moreover, no additional peak corresponding to W-O-W bond (813-830 cm^{-1} in the FTIR spectra, and 273, 329, 720, and 809 cm^{-1} in Raman spectra) was observed [43,74]. These findings suggest that the tungsten species did not form a separate phase such as WO_3, rather being incorporated into the MoV structure in substitutional manner. As the amount of tungsten in the catalysts became higher, peaks related to molybdenum-oxygen and vanadium-oxygen bonds became smaller while peaks arising from tungsten-oxygen bonds became dominant.

Figure 2-11 shows XANES spectra around the W L_1-edge region. The local geometry of tungsten can be determined by the pre-edge of the W L_1-edge region [75]. The pre-edge peak at the W L_1-edge, caused by a $2s \rightarrow 5d$ transition, shows a significant intensity in the case of tetrahedral symmetry while small or no peaks are obtained in octahedral symmetry [75]. The

MoVW catalysts exhibited a small pre-edge peak in the W L_1-edge region, indicating that incorporated tungsten species have distorted octahedral units, which is the same tungsten coordinates with MoVW models (Figure 2-2). MoVW-1 showed a relatively distinct peak compared to a sample of the reference catalyst (WO_3). As the tungsten content increased, the peak became smaller, and analogous to that of WO_3. It was found that octahedrons in MoVW-1 were more distorted than that of the others, and the degree of distortion was decreased with increasing tungsten content. Combination with previous energetics for incorporation of tungsten, it is confirmed that tungsten was located at molybdenum or vanadium positions with octahedral coordinates in MoV structure.

2.3.3 Effect of incorporated tungsten on acid and redox properties

The above findings clearly indicate that MoVW catalysts were successfully developed and that their structures were similar to those for models designed by DFT. It therefore appears that chemical interactions among molybdenum, vanadium, tungsten and oxygen occur, as previously calculated. NH_3-TPD, XPS, and H_2-TPR were employed to investigate changes in the intrinsic properties of the samples, such as acid properties, the oxidation state of the metal components, and lattice oxygen, which facilitates the dehydration of glycerol and the selective oxidation of acrolein.

NH_3-TPD analysis was performed to investigate the effect of tungsten on the acid properties of the sample. As shown in Figure 2-12 and Table 2-11,

the MoVW catalysts were confirmed to possess a higher number of acid sites than the MoV catalyst (0.259 mmol/g). The amount of acid increased from MoVW-1 (0.260 mmol/g) to MoVW-5 (0.485 mmol/g), and decreased from it to MoVW-9 (0.270 mmol/g). Note that, NH_3 desorption peak was located below 200 ^oC in the MoV sample, suggesting a low acid strength. As tungsten was incorporated, additional shoulders around 300 ^oC appeared. This indicates that acid sites with a high acid strength were generated by the presence of tungsten. It can be attributed to the high electronegativity of tungsten compared to that of molybdenum and vanadium [76]. This enhancement in acid properties would enhance the conversion of glycerol to acrolein, the first step in the oxydehydration of glycerol.

To understand effect of incorporated tungsten on the oxidation state of molybdenum and vanadium atoms, the MoV and MoVW catalysts were investigated by means of an XPS technique. As shown in Table 2-12, for MoV sample, most of the molybdenum atoms were present in a high oxidation state (Mo^{6+}). Both V^{4+} and V^{5+} were observed in the catalyst, with a $V^{4+}/(V^{4+}+V^{5+})$ ratio of 0.667. The oxidation state of molybdenum and vanadium in the MoVW catalysts was significantly changed by the addition of tungsten. The ratio of $Mo^{5+}/(Mo^{5+}+Mo^{6+})$ was increased from 0 to 0.266 when the tungsten content increased. The $V^{4+}/(V^{4+}+V^{5+})$ ratio was also increased from 0.667 in the MoV catalyst to 0.750 in MoVW-5, and decreased to 0.694 in MoVW-9. In the case of tungsten atoms, oxidized species (W^{6+}) were dominant regardless of tungsten fraction. That is, when tungsten was incorporated into the MoV framework, Mo^{6+} and V^{5+} were

reduced to Mo^{5+} and V^{4+} while tungsten ions were in an oxidized state (W^{6+}). Interestingly, the result that tungsten induces reduced states of molybdenum and vanadium in XPS, is good agreement with previous DFT calculation (charge density differences and Bader charge analysis). It demonstrates the validity of designed MoVW models by DFT. In comparison with results of Bader charge analysis (Table 2-9), similar trend according to tungsten contents was obtained, except in MoVW-7 catalyst. The reason for this, we suggest, is that MoVW-7 catalyst exhibited more disordered a-b plane than other catalysts due to high content of tungsten (Figure 2-6).

H_2-TPR was performed to study reducibility of the samples (Figure 2-13). The performance of a selective oxidation catalyst is closely related to the reducibility of the lattice oxygen in the catalysts [77-79]. A broad peak was observed for the MoV sample in the range of 450-650 ^{o}C. This can be attributed to complex molybdenum and vanadium mixed oxide species, not V_2O_5 and MoO_3 [80]. Compared to the MoV sample, peaks of the MoVW samples were shifted toward lower temperatures. The peaks were not exactly defined, but it was certain that a weaker metal-oxygen interaction was induced as the result of the incorporation of tungsten into MoV framework. That is to say, tungsten-containing samples were able to easily release solid oxygen species, resulting in the highly selective conversion of acrolein to acrylic acid.

2.3.4 Effect of reaction temperature and contact time on activity

The dehydration of glycerol is an endothermic reaction whereas the oxidation of acrolein is an exothermic reaction [42]. In addition, the two reactions have different optimal reaction temperature. Accordingly, it is worthy to trace product distributions over bi-functional catalyst as a function of reaction temperature. Figure 2-14 shows catalytic test results for different reaction temperatures. The conversion of glycerol was complete over the range of temperatures used. It is still worth comparing product selectivities in full conversion of glycerol because it is consecutive reactions [81]. The highest selectivity for acrylic acid was observed at 250 ^{o}C. When reaction temperature reached 275 ^{o}C, the selectivity for acrylic acid was reduced by more than half (13.5%). In addition, primary products (acetaldehyde, acrolein, etc.) were rarely detected. The results imply that reactant and products were unselectively oxidized to CO and CO_2 (66.7%) at high reaction temperature. A further increase in temperature from 275 to 350 ^{o}C led to a progressive decline in selectivity for acrylic acid (ca. 3%), and a significant increase in CO_x up to 80.7%. The higher selectivity for acetic acid could be the result of the oxidation of acetaldehyde and the cleavage of the C-C bond of acetol and acrylic acid by activation of acid sites respectively at temperatures higher than 250 ^{o}C [82].

Generally in a long contact time, acrolein production from glycerol is facilitated over acid sites whereas selectivity from acrolein to acrylic acid is decreased over oxidation sites. On the other hand, in the case of a short

contact time, the opposite tendency was observed [83,84]. Hence, the contact time, not only of the reactant (glycerol) but also the intermediate (acrolein) should be optimized for the acrylic acid production. The effect of contact time on the product distribution of glycerol oxydehydration over the MoVW-5 catalyst was investigated at 250 ^{o}C (Figure 2-15). The test was performed with varying amounts of catalyst with the same feed rate. Even at a short contact time (0.05 s), the conversion of glycerol was complete. Primary products (acrolein and acetaldehyde), secondary products (acrylic acid and acetic acid), and total oxidation products (CO and CO_2) were detected. When the contact time reached 0.16 s, selectivity for acrylic acid increased from 22.2% to 28.7% and CO_x production was decreased from 42.5% to 37.1% compared to contact time of 0.05 s. This can be interpreted as a lack opportunity for reactants and intermediates to come into contact with acid sites and oxidation sites, respectively, at a short contact time can stimulate undesired reaction to produce by-products. On the other hand, at a contact time of 0.16 s, as the dehydration of acrolein and the consecutive selective oxidation of acrolein were balanced, a high yield of acrylic acid with a low yield of by-products were observed. As the contact time was increased (> 0.2 s), selectivity for CO_x significantly increased, reaching 53.1% at 0.27 s, and the selectivity for acrylic acid was simultaneously decreased. Primary products were not observed and acetic acid was increased. Considering the results, increase chance to contact reactant and products with vanadium species, well known as redox sites [69], stimulates the transformation of

primary products into secondary product and enhances the total oxidation of products.

2.3.5 Effect of tungsten on catalytic activity for oxydehydration of glycerol

To clarify the effect of incorporated tungsten on catalytic performance for the oxydehydration of glycerol, we compared the physically mixed catalyst (WO_3 and MoV) and MoVW-5. WO_3 was prepared by the same procedure as previously reported, showing a high yield of acrolein [43]. To load the physically mixed catalysts with the same moles of molybdenum, vanadium, and tungsten corresponding to 0.3 g of MoVW-5 catalyst, we calculated the weight of the WO_3 and MoV catalysts based on EPMA results (Table 2-11). Figure 2-16 shows the results for the oxydehydration of glycerol over both catalytic systems. Full conversion and a similar yield of acetaldehyde and acetic acid (denoted 'others') were obtained in both systems. However, the selectivity for acrylic acid over MoVW-5 was almost twice as that over the WO_3 and MoV mixture. In addition, much lower production of CO_x was observed over MoVW-5 compared to the physical mixture of WO_3 and MoV catalysts. If separate phase of MoV and WO_x was formed in MoVW-5, the reaction results would be similar to a physical mixture system. From this, we clarified that tungsten species are incorporated into the MoV framework, thus enhancing acid and redox properties. It was also found that total oxidation was suppressed by the presence of tungsten, resulting in an enhancement in selectivity for acrylic acid.

The catalytic performance for the oxydehydration of glycerol over the MoVW catalysts with different tungsten fractions is presented in Table 2-13. For comparison, MoV catalyst without tungsten was also tested. Full glycerol conversion was obtained over all of the catalysts. The catalyst without tungsten (MoV), exhibited extremely high selectivity for CO_x (66.2%) with a low production of acrylic acid (12.4%). Over the MoVW-1 catalyst, although even a small amount of tungsten was present, selectivity for acrylic acid was significantly increased from 12.4% to 21.7%. Products corresponding to the complete oxidation (CO_x) were also remarkably decreased from 66.2% to 50.9%. In addition, unconverted acrolein was obtained in contrast to the results for MoV catalyst. The physicochemical properties of the MoVW-1 catalyst, such as surface area, acid amounts, and crystal structure, were similar to those for the MoV catalyst (Table 2-11). The main differences were the oxidation state of metal atoms and reducibility. Taking this account, the high reducibility and the reduced oxidation state of metal atoms caused by the incorporation of tungsten are reasons why the MoVW-1 catalyst showed higher selectivity for acrylic acid than MoV catalyst.

As the tungsten content in MoVW catalysts was increased, the selectivity of acrylic acid was increased from MoVW-1 (21.7%) to MoVW-5 (30.5%) with a significant decrease in CO_x production (35.6%). With a further increase in the tungsten fraction to MoVW-7, CO_x selectivity was slightly increased whereas acrylic acid selectivity was decreased. In the case of MoVW-9, with hexagonal tungsten bronze structure (Figure 2-6), selectivity for acrylic acid

(12.6%) was comparable with that of the MoV catalyst. In addition, large amounts of unconverted acrolein and acetaldehyde were observed, indicating that its characteristic structure (hexagonal tungsten bronze) is less active for the selective oxidation than the MoV phase. This suggests that the MoV phase is necessary for the efficient conversion of acrolein to acrylic acid in glycerol oxydehydration, and the maintenance of its structure even with incorporation of tungsten is crucial for functioning as an efficient bi-functional catalyst.

For a clear understanding of product variation with different compositions, the total yield of acrolein and acrylic acid, acid amounts, selectivity of CO_x in oxidation products, and ratios of $V^{4+}/(V^{4+}+V^{5+})$ were plotted as a function of tungsten content (Figure 2-17). To exclude the effect of structure, catalysts with MoV structure were included (MoVW-1 to 7). Acid amount exhibited similar trend of total production of acrolein and acrylic acid along with tungsten content, and also showed a maximum peak at the same tungsten content of 5 (Figure 2-17A). Hence, high acid density can be advantageous for producing acrylic acid, confirming acrylic acid is produced from glycerol via acrolein.[8,26] In Figure 2-17B, we used "selectivity in oxidation products (acrylic acid, acetic acid, and CO_x)" to clarify influence of oxidation states of vanadium atoms on oxidation product distributions. As the tungsten content increased, the ratio of $V^{4+}/(V^{4+}+V^{5+})$ was increased to MoVW-5, and decreased to MoVW-7. Interestingly, an opposite trend was obtained in a plot of CO_x selectivity in oxidation products with tungsten content. This indicates that the ratio of $V^{4+}/(V^{4+}+V^{5+})$ is a crucial determinant

of selectivity for acrylic acid and CO_x, and V^{4+} is favorable for converting acrolein into acrylic acid rather than CO_x. Consequently, it was confirmed that high acid properties and ratio of $V^{4+}/(V^{4+}+V^{5+})$ of MoVW-5 catalyst resulted in the highest selectivity for acrylic acid among the catalysts tested. Furthermore, it is obvious that introduced tungsten played a role, not only as an acidic species but also a promoter to suppress total oxidation by reducing the vanadium species

2.3.6 Effect of tungsten on catalytic stability of MoVW catalyst

For an investigation of the effect of tungsten on the stability of the MoVW catalyst, XPS analysis and long-term catalytic tests were carried out. In previous research, the deactivation of bi-functional catalysts was mainly reported to be caused by a change in the oxidation state of the redox center rather than acid sites [43]. To address this issue, we employed XPS analysis to compare the oxidation state of metal atoms in MoV and MoVW catalysts before and after the reactions (Table 2-12). For both MoV and MoVW catalysts, vanadium atoms were oxidized after the reaction while other metal ions were rarely changed. This suggests that vanadium works as a redox center. In MoV catalyst, the ratio of $V^{4+}/(V^{4+}+V^{5+})$ was decreased remarkably from 0.667 to 0.599. On the other hand, only small portion of V^{4+} was oxidized to V^{5+} in the MoVW catalysts. Instead, molybdenum and tungsten were slightly oxidized. That is, V^{4+} was stabilized in the presence of

tungsten species. This can results in a high catalytic stability of MoVW catalysts for oxydehydration of glycerol.

Figure 2-18 shows results of long-term stability tests over the MoVW-5 catalyst. At the initial point (1 h), yield of CO_x was over 40% and, the yield of acrylic acid was below 25% with the complete conversion of glycerol. With passing time, it appears that the catalyst was activated by the feed including reactants and O_2. At 14 h, the production of CO_x was decreased to ca. 36%, and the highest selectivity of acrylic acid (30.5%) was recorded. During a 110 h reaction, the complete conversion of glycerol and high acrylic acid yield (above 30%) were maintained. The total amount of acrolein and acrylic acid remained unchanged during the test, which could mean that no severe deactivation of acid sites had occurred. This stable behavior of MoVW-5 was contributed to high coke resistance due to its low acid strength [34], and stabilization of the oxidation states of vanadium by the presence of tungsten species.

2.3.7 Comparative activity test in two-bed system

To demonstrate the potential of MoVW catalysts in practical applications, we performed catalytic tests with an additional acid catalyst bed. Two separate beds system was formed by laying conventional acid catalyst (HZSM-5, Si/Al=40) on MoV and MoVW-5 catalysts. This system was proven to be effective for maximizing acrylic acid production because the undesirable oxidation of glycerol can be avoided by the complete conversion

of glycerol over the first bed. The results are listed in Table 2-14. Separate sequential beds of HZSM-5 and MoV catalysts gave a 100% glycerol conversion and a 32.4% selectivity for acrylic acid. This is comparable to the value obtained for the MoVW-5 single bed system. Interestingly, in the HZSM-5 and MoVW-5 catalysts beds system, much higher selectivity for acrylic acid (47.2%) was obtained with the full conversion of glycerol. This performance was also confirmed to be higher than previous results in which a two-layered system was used. In addition, a remarkably low selectivity for CO and CO2 was found compared to MoV based system, indicating that the MoVW-5 catalyst is more selective for the conversion of acrolein to acrylic acid than the MoV catalyst. When the outstanding stability and selectivity for acrylic acid of the MoVW catalyst system are taken into consideration, we conclude that MoVW catalysts have potential for use in practical applications.

Table 2-1. DFT-calculated substitutional and interstitial insertion energies of tungsten into various positions in MoV structure.

Type	Position	Insertion energy of W (eV)
Substitutional insertion (E_S)	Mo1	-1.11
	Mo2	-1.11
	Mo3	-1.08
	Mo4	-1.13
	Mo5	-0.95
	Mo6	-1.11
	Mo7	-1.19
	V1	-0.48
	V2	-0.44
	V3	+0.07
Interstitial insertion (E_I)	H1	+0.00
	H2	+1.97

Table 2-2. Probability of substitution of tungsten for molybdenum and vanadium at various positions in MoV model.

Atom	Position	Probability[a] (%)
Mo	Mo1	7.6
	Mo2	7.6
	Mo3	3.5
	Mo4	12.8
	Mo5	0.2
	Mo6	7.6
	Mo7	60.7
V	V1	73.8
	V2	26.2
	V3	0.0

[a] Probability (P_i) of substitution of tungsten for molybdenum and vanadium at various positions was calculated by following equation:

$$P_i = \frac{1}{Z}\exp\left(-\frac{\Delta E_i}{kT}\right)$$

where k = 8.6173 × 10^{-5} eV K^{-1} is Boltzmann's constant, E_i is the substitutional energy of tungsten for molybdenum and vanadium at various positions in MoV model, T = 448 K is synthesis temperature of MoVW catalyst, and

$$Z = \sum_{i=1}^{N} \exp\left(-\frac{\Delta E_i}{kT}\right)$$

is normalization factor.

Table 2-3. Energy and probability of substitution of tungsten for molybdenum and vanadium at various positions in MoVW-1 model.

Atom	Position	Substitution energy[a] (eV)	Probability[b] (%)
Mo	Mo1	-1.04	14.3
	Mo2	-1.04	14.3
	Mo3	-1.01	6.6
	Mo4	-1.08	40.4
	Mo5	-0.89	0.3
	Mo6	-1.06	24.1
V	V1	-0.49	98.4
	V2	-0.33	1.6
	V3	0.18	0

[a] Substitution energy of a tungsten atom in MoVW-1 model was calculated by following equation:

$E_S = (E_{W\ sub\text{-}MoVW\text{-}1} + E_{Mo\ or\ V}) - (E_{MoVW\text{-}1} + E_W)$

where $E_{W\ sub\text{-}MoVW\text{-}1}$ is bulk energy of MoVW-1 unit cell in which one tungsten atom is substituted for molybdenum or vanadium atom, $E_{MoVW\text{-}1}$ is bulk energy of most stable MoVW-1 unit cell, $E_{Mo,\ V,\ or\ W}$ is the bulk energy of the corresponding metal per atom.

[b] Probability (P_i) of substitution of tungsten for molybdenum and vanadium at various positions was calculated by following equation:

$$P_i = \frac{1}{Z}\exp\left(-\frac{\Delta E_i}{kT}\right)$$

where $k = 8.6173 \times 10^{-5}$ eV K^{-1} is Boltzmann's constant, E_i is the substitutional energy of tungsten for molybdenum and vanadium at various positions in MoVW-1 model, $T = 448$ K is synthesis temperature of MoVW catalyst, and

$$Z = \sum_{i=1}^{N} \exp\left(-\frac{\Delta E_i}{kT}\right)$$

is normalization factor.

Table 2-4. Energy and probability of substitution of tungsten for molybdenum and vanadium at various positions in MoVW-3 model.

Atom	Position	Substitution energy[a] (eV)	Probability[b] (%)
Mo	Mo1	-1.08	38.8
	Mo2	-1.07	29.9
	Mo3	-1.02	8.2
	Mo5	-0.80	0.0
	Mo6	-1.06	23.1
V	V2	-0.17	100.0
	V3	+0.19	0.0

[a] Substitution energy of a tungsten atom in MoVW-3 model was calculated by following equation:

$E_S = (E_{W\ sub\text{-}MoVW\text{-}3} + E_{Mo\ or\ V}) - (E_{MoVW\text{-}3} + E_W)$

where $E_{W\ sub\text{-}MoVW\text{-}3}$ is bulk energy of MoVW-3 unit cell in which one tungsten atom is substituted for molybdenum or vanadium atom, $E_{MoVW\text{-}3}$ is bulk energy of most stable MoVW-3 unit cell, $E_{Mo,\ V,\ or\ W}$ is the bulk energy of the corresponding metal per atom.

[b] Probability (P_i) of substitution of tungsten for molybdenum and vanadium at various positions was calculated by following equation

$$P_i = \frac{1}{Z}\exp\left(-\frac{\Delta E_i}{kT}\right)$$

where k = 8.6173 × 10^{-5} eV K^{-1} is Boltzmann's constant, E_i is the substitutional energy of tungsten for molybdenum and vanadium at various positions in MoVW-3 model, T = 448 K is synthesis temperature of MoVW catalyst, and

$$Z = \sum_{i=1}^{N}\exp\left(-\frac{\Delta E_i}{kT}\right)$$

is normalization factor.

Table 2-5. Formation energies and probabilities for various configurations of MoVW-1.

Configuration	The number of atoms substituted by tungsten atoms		Formation energy[a] (eV)	Probability of formation for configuration[b] (%)
	Mo7	Mo4		
MoVW-1 (1)	4	0	-4.51	72.4
MoVW-1 (2)	3	1	-4.46	18.0
MoVW-1 (3)	2	2	-4.41	5.6
MoVW-1 (4)	1	3	-4.40	3.8
MoVW-1 (5)	0	4	-4.29	0.2

[a] Formation energy of configuration m ($E_{f,m}$) was calculated by following equation:

$E_{f,m} = (E_{total,m} + aE_{Mo} + bE_V) - (E_{MoV} + cE_W)$

where $E_{total,m}$ is bulk energy of configuration m for MoVW-1, E_{MoV} is bulk energy of MoV unit cell, $E_{Mo,\ V,\ or\ W}$ is the bulk energy of the corresponding metal per atom, a and b are the number of molybdenum and vanadium atoms substituted by tungsten atoms, and c is the number of tungsten atoms substituted for molybdenum and vanadium atoms.

[b] Probability of formation for configuration m (P_m) was calculated by following equation:

$$P_m = \frac{1}{Z}\exp\left(-\frac{\Delta E_{f,m}}{kT}\right)$$

where $k = 8.6173 \times 10^{-5}$ eV K^{-1} is Boltzmann's constant, $E_{f,m}$ is the formation energy of configuration m, $T = 448$ K is synthesis temperature of MoVW-1 catalyst, and

$$Z = \sum_{m=1}^{N} \exp\left(-\frac{\Delta E_{f,m}}{kT}\right)$$

is normalization factor.

Table 2-6. Formation energies and probabilities for various configurations of MoVW-3 model.

Configuration	The number of atoms substituted by tungsten atoms			Formation energy[a] (eV)	Probability of formation for configuration[b] (%)
	Mo4	Mo6	V1		
MoVW-3 (1)	4	0	2	-5.20	52.1
MoVW-3 (2)	3	1	2	-5.18	31.1
MoVW-3 (3)	2	2	2	-5.15	14.3
MoVW-3 (4)	1	3	2	-5.08	2.3
MoVW-3 (5)	0	4	2	-4.98	0.2

[a] Formation energy of configuration m ($E_{f,m}$) was calculated by following equation:

$E_{f,m} = (E_{total,m} + aE_{Mo} + bE_V) - (E_{MoVW-1} + cE_W)$

where $E_{total,m}$ is bulk energy of configuration m for MoVW-3, E_{MoVW-1} is bulk energy of most stable MoVW-1 unit cell, $E_{Mo,\ V,\ or\ W}$ is the bulk energy of the corresponding metal per atom, a and b are the number of molybdenum and vanadium atoms substituted by tungsten atoms, and c is the number of tungsten atoms substituted for molybdenum and vanadium atoms.

[b] Probability of formation for configuration m (P_m) was calculated by following equation:

$$P_m = \frac{1}{Z}\exp\left(-\frac{\Delta E_{f,m}}{kT}\right)$$

where $k = 8.6173 \times 10^{-5}$ eV K^{-1} is Boltzmann's constant, $E_{f,m}$ is the formation energy of configuration m, $T = 448$ K is synthesis temperature of MoVW-3 catalyst, and

$$Z = \sum_{m=1}^{N} \exp\left(-\frac{\Delta E_{f,m}}{kT}\right)$$

is normalization factor.

Table 2-7. Formation energies and probabilities for various configurations of MoVW-5 model.

Configuration	The number of atoms substituted by tungsten atoms				Formation energy[a] (eV)	Probability of formation for configuration[b] (%)
	Mo1	Mo2	Mo6	V2		
MoVW-5 (1)	3	0	0	2	-3.53	24.4
MoVW-5 (2)	0	3	0	2	-3.52	18.8
MoVW-5 (3)	0	0	3	2	-3.37	0.4
MoVW-5 (4)	2	1	0	2	-3.50	11.2
MoVW-5 (5)	2	0	1	2	-3.46	4.4
MoVW-5 (6)	1	2	0	2	-3.52	18.8
MoVW-5 (7)	0	2	1	2	-3.49	9.8
MoVW-5 (8)	1	0	2	2	-3.39	0.7
MoVW-5 (9)	0	1	2	2	-3.36	0.3
MoVW-5 (10)	1	1	1	2	-3.50	11.2

[a] Formation energy of configuration m ($E_{f,m}$) was calculated by following equation:

$E_{f,m} = (E_{total,m} + aE_{Mo} + bE_V) - (E_{MoVW-3} + cE_W)$

where $E_{total,m}$ is bulk energy of configuration m for MoVW-5, E_{MoVW-3} is bulk energy of most stable MoVW-3 unit cell, $E_{Mo,\ V,\ or\ W}$ is the bulk energy of the corresponding metal per atom, a and b are the number of molybdenum and vanadium atoms substituted by tungsten atoms, and c is the number of tungsten atoms substituted for molybdenum and vanadium atoms.

[b] Probability of formation for configuration m (P_m) was calculated by following equation:

$$P_m = \frac{1}{Z}\exp\left(-\frac{\Delta E_{f,m}}{kT}\right)$$

where $k = 8.6173 \times 10^{-5}$ eV K^{-1} is Boltzmann's constant, $E_{f,m}$ is the formation energy of configuration m, $T = 448$ K is synthesis temperature of MoVW-5 catalyst, and

$$Z = \sum_{\mathrm{m}=1}^{N} \exp\left(-\frac{\Delta E_{\mathrm{f,m}}}{kT}\right)$$

is normalization factor.

Table 2-8. Formation energies and probabilities for various configurations of MoVW-7 model.

Configuration	The number of atoms substituted by tungsten atoms				Formation energy[a] (eV)	Probability of formation for configuration[b] (%)
	Mo1	Mo2	Mo6	V2		
MoVW-7 (1)	1	1	0	1	-1.99	47.4
MoVW-7 (2)	1	0	1	1	-1.94	13.0
MoVW-7 (3)	0	1	1	1	-1.93	10.0
MoVW-7 (4)	0	2	0	1	-1.97	28.3
MoVW-7 (5)	0	0	2	1	-1.85	1.3

[a] Formation energy of configuration m ($E_{f,m}$) was calculated by following equation:

$E_{f,m} = (E_{total,m} + aE_{Mo} + bE_V) - (E_{MoVW\text{-}5} + cE_W)$

where $E_{total,m}$ is bulk energy of configuration m for MoVW-7, $E_{MoVW\text{-}5}$ is bulk energy of most stable MoVW-5 unit cell, $E_{Mo,\ V,\ or\ W}$ is the bulk energy of the corresponding metal per atom, a and b are the number of molybdenum and vanadium atoms substituted by tungsten atoms, and c is the number of tungsten atoms substituted for molybdenum and vanadium atoms.

[b] Probability of formation for configuration m (P_m) was calculated by following equation:

$$P_m = \frac{1}{Z}\exp\left(-\frac{\Delta E_{f,m}}{kT}\right)$$

where $k = 8.6173 \times 10^{-5}$ eV K^{-1} is Boltzmann's constant, $E_{f,m}$ is the formation energy of configuration m, $T = 448$ K is synthesis temperature of MoVW-7 catalyst, and

$$Z = \sum_{m=1}^{N} \exp\left(-\frac{\Delta E_{f,m}}{kT}\right)$$

is normalization factor.

Table 2-9. Average oxidation state of molybdenum, vanadium, and tungsten in MoV and MoVW catalysts, calculated by Bader charge analysis

Catalyst	Calculated oxidation state		
	Mo	V	W
MoV	+3.63	+2.58	-
MoVW-1	+3.61	+2.58	+4.52
MoVW-3	+3.55	+2.56	+4.54
MoVW-5	+3.51	+2.50	+4.48
MoVW-7	+3.45	+2.50	+4.49

Table 2-10. Experimental and calculated lattice constant of [100] direction (c-direction) of MoV and MoVW catalysts

Catalyst	d (Å)	
	Experimental (XRD)	Calculated (DFT)
MoV	3.995	4.097
MoVW-1	3.991	4.071
MoVW-3	3.946	4.023
MoVW-5	3.934	3.984
MoVW-7	3.907	3.956

Table 2-11. Physicochemical properties of the MoV and MoVW catalysts

Catalyst	Specific Surface area[a] (m^2/g)	Acid amount[b] (mmol/g)	Relative bulk compositions[c] (Mo/V/W)	Surface compositions[d] (Mo/V/W/O)	Crystal structure[e]
MoV	21.2	0.259	2.6/1.0/0.0	24.2/5.2/0.0/70.6	Amorphous
MoVW-1	22.8	0.260	2.4/1.0/0.4	19.1/3.4/7.9/69.6	Amorphous
MoVW-3	36.8	0.438	2.8/1.0/1.4	15.1/2.4/12.3/70.2	Amorphous
MoVW-5	25.0	0.485	3.2/1.0/2.5	12.3/1.7/16.1/70.0	Amorphous
MoVW-7	22.2	0.321	3.0/1.0/3.4	10.0/1.4/18.0/70.5	Amorphous
MoVW-9	17.4	0.270	3.0/1.0/5.6	7.7/1.1/19.3/71.9	Hexagonal tungsten bronze

[a] Specific surface area was determined from the N_2 adsorption branch.

[b] The amount of acid sites was evaluated based on NH_3 temperature-programmed desorption (NH_3-TPD).

[c] Elemental compositions of solid catalysts were determined by EPMA.

[d] Surface composition was obtained by XPS analysis.

[e] Crystalline structure was determined by XRD analysis.

Table 2-12. Oxidation state of molybdenum, vanadium, and tungsten in MoV and MoVW catalysts before and after reaction[a]

Catalyst	Before reaction			After reaction[b]		
	$Mo^{5+}/(Mo^{5+}+Mo^{6+})$	$V^{4+}/(V^{4+}+V^{5+})$	$W^{5+}/(W^{5+}+W^{6+})$	$Mo^{5+}/(Mo^{5+}+Mo^{6+})$	$V^{4+}/(V^{4+}+V^{5+})$	$W^{5+}/(W^{5+}+W^{6+})$
MoV	0.000	0.667	-	0.000	0.599	-
MoVW-1	0.000	0.674	0.019	0.007	0.660	0.016
MoVW-3	0.084	0.695	0.042	0.091	0.691	0.005
MoVW-5	0.234	0.750	0.051	0.230	0.740	0.015
MoVW-7	0.260	0.712	0.038	0.232	0.679	0.000
MoVW-9	0.266	0.694	0.082	0.255	0.668	0.062

[a] Binding energy: Mo^{5+} ($3d_{5/2}$ = 231.7 ± 0.2 eV, $3d_{3/2}$ = 234.8 ± 0.2 eV), Mo^{6+} ($3d_{5/2}$ = 232.8 ± 0.2 eV, $3d_{3/2}$ = 235.9 ± 0.2 eV), V^{4+} ($2p_{3/2}$ = 516.7 ± 0.2 eV), V^{5+} ($2p_{3/2}$ = 517.7 ± 0.2 eV), W^{5+} ($4f_{7/2}$ = 35.0 ± 0.2 eV, $4f_{5/2}$ = 37.1 ± 0.2 eV), W^{6+} ($4f_{7/2}$ = 35.6 ± 0.2 eV, $4f_{5/2}$ = 37.7 ± 0.2 eV).

[b] Reaction condition: catalyst amount 0.3 g; reaction temperature 250 °C; total feed rate 74.34 mL min^{-1}; feed composition (vol.%) glycerol/O_2/H_2O/N_2/He=1.3/2.6/55.1/37.0/3.9. The catalysts were collected after 14 h time-on-stream reaction.

Table 2-13. Conversion and selectivities of MoV and MoVW catalysts with various tungsten contents[a]

Catalyst	Glycerol conversion (%)	Selectivity (%)				
		Acrylic acid	Acrolein	Acetic acid	CO_x	Acetaldehyde
MoV	100	12.4	0.0	8.6	66.2	<1.0
MoVW-1	100	21.7	2.0	8.4	50.9	<1.0
MoVW-3	100	23.2	2.1	8.8	48.0	<1.0
MoVW-5	100	30.5	8.2	8.5	35.6	3.3
MoVW-7	100	21.3	9.4	7.0	38.7	3.6
MoVW-9	100	12.6	20.0	5.6	34.6	5.6

[a] Reaction condition: catalyst amount 0.3 g; reaction temperature 250 ^{o}C; total feed rate 74.34 mL min^{-1}; feed composition (vol.%) glycerol/O_2/H_2O/N_2/He=1.3/2.6/55.1/37.0/3.9. The reaction results were taken after 14 h time-on-stream.

Table 2-14. Comparative conversion and selectivities of two separate bed systems with HZSM (1st layer), and MoV and MoVW-5 catalysts (2nd layer)[a]

Catalyst	Glycerol conversion (%)	Selectivity (%)				
		Acrylic acid	Acrolein	Acetic acid	CO_x	Acetaldehyde
HZSM-5 + MoV	100	32.4	0.0	10.3	55.6	<1.0
HZSM-5 + MoVW-5	100	47.2	0.3	9.8	39.4	<1.0

[a] Reaction condition: reaction temperature 250 ^{o}C; total feed rate 74.34 mL min^{-1}; feed composition (vol.%) glycerol/O_2/H_2O/N_2/He=1.3/2.6/55.1/37.0/3.9. The reaction results were taken after 2 h time-on-stream. Two layer catalyst system: 1st layer: HZSM-5 (0.05g); 2nd layer: MoV or MoVW-5 catalyst (0.3 g).

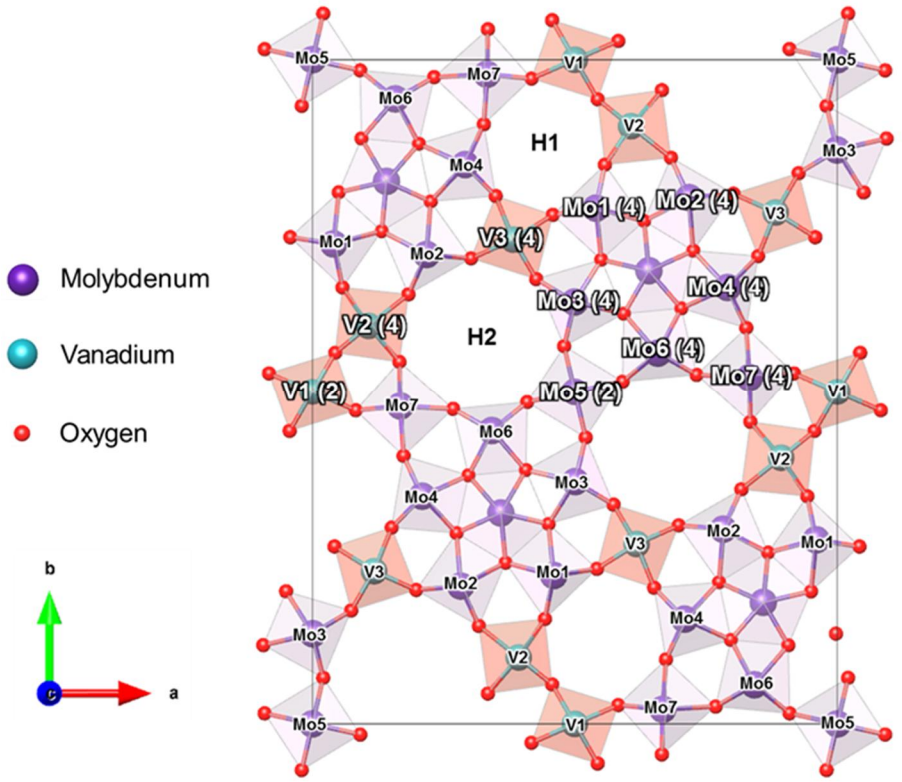

Figure 2-1. Incorporation sites of tungsten species in the MoV structure (Top view of MoV structure). The atomic coordinates are taken from previous report. Value in parenthesis indicates total number of each site in unit cell.

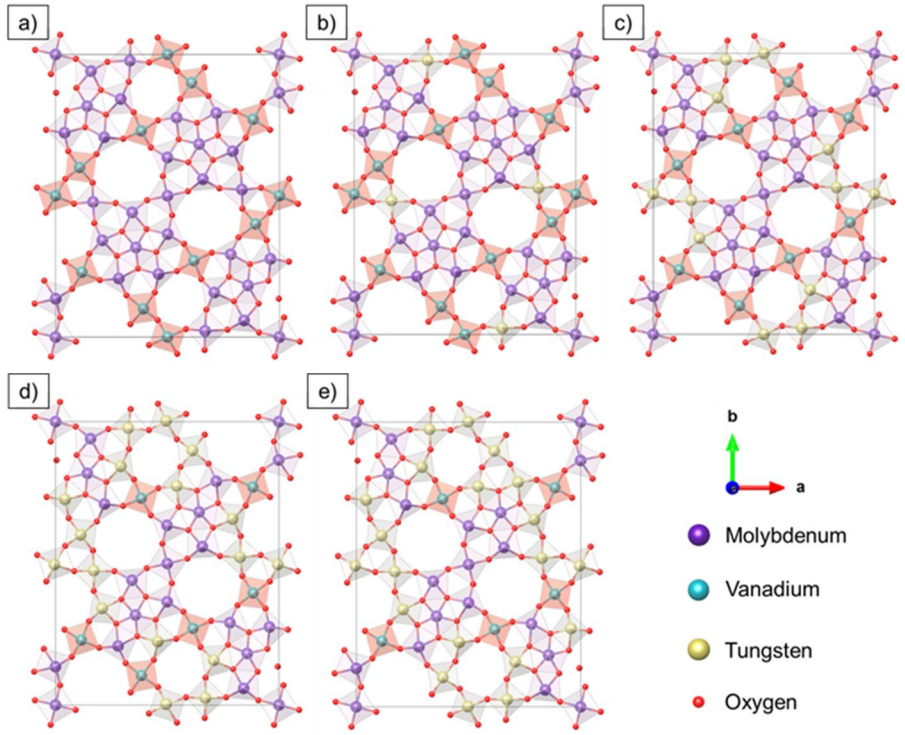

Figure 2-2. Calculation models (1×1×1) of a) MoV, b) MoVW-1, c) MoVW-3, d) MoVW-5, and e) MoVW-7 catalysts viewed from [001] direction. Rectangles in each model indicate a primitive unit cell.

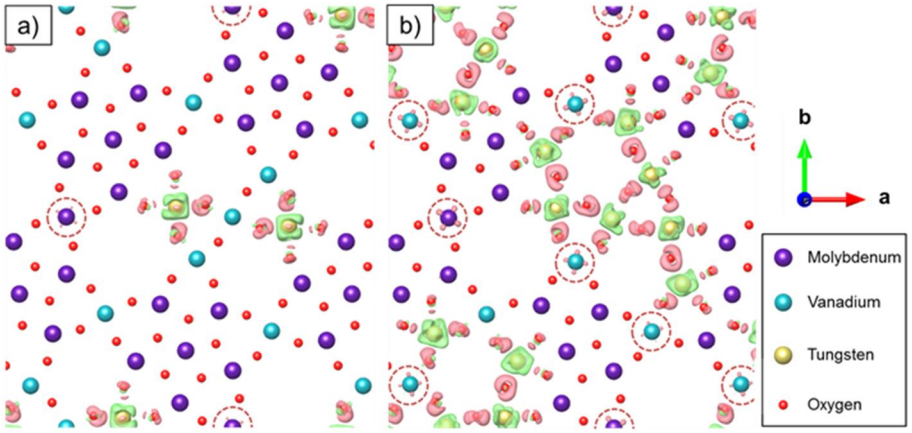

Figure 2-3. Calculated charge density differences for a) MoVW-1 and b) MoVW-5. Green color indicates a loss of electrons while pink shows a gain of electrons. Isosurface: 0.018.

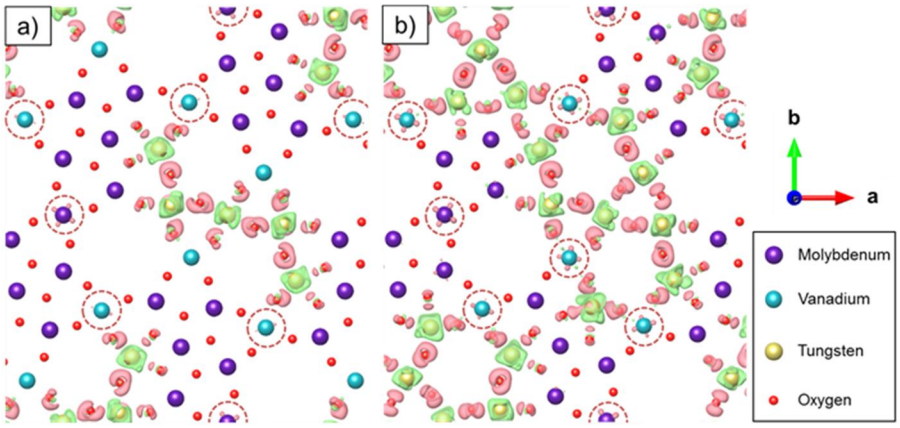

Figure 2-4. Calculated charge density differences for a) MoVW-3 and b) MoVW-7. Green color indicates a loss of electrons while pink shows a gain of electrons. Isosurface: 0.018.

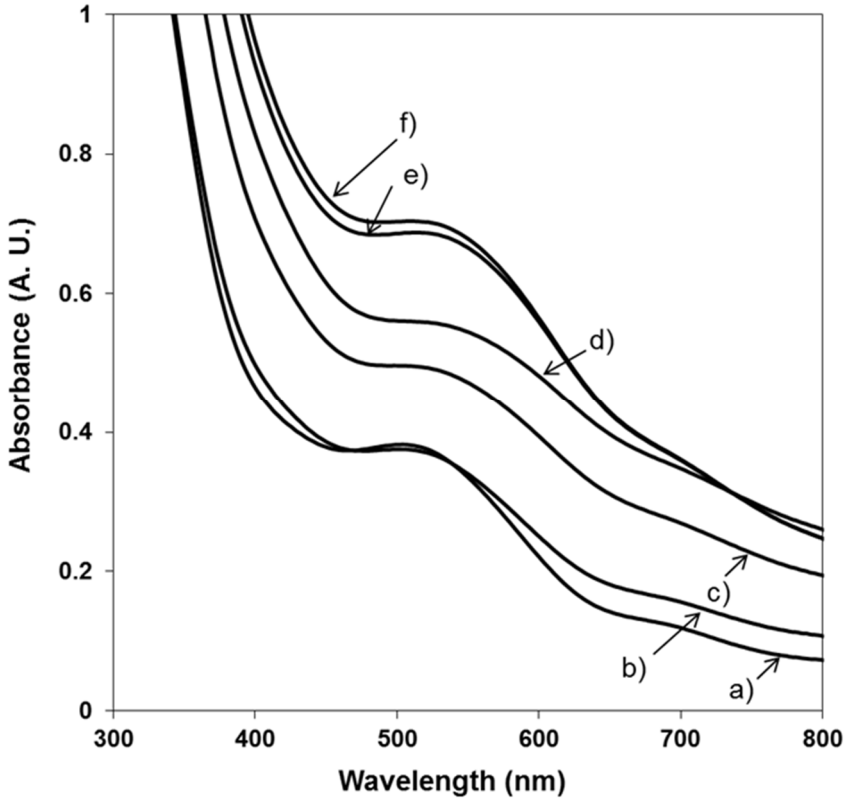

Figure 2-5. UV-vis spectra of diluted a) MoV, b) MoVW-1, c) MoVW-3, d) MoVW-5, e) MoVW-7, and f) MoVW-9 solutions.

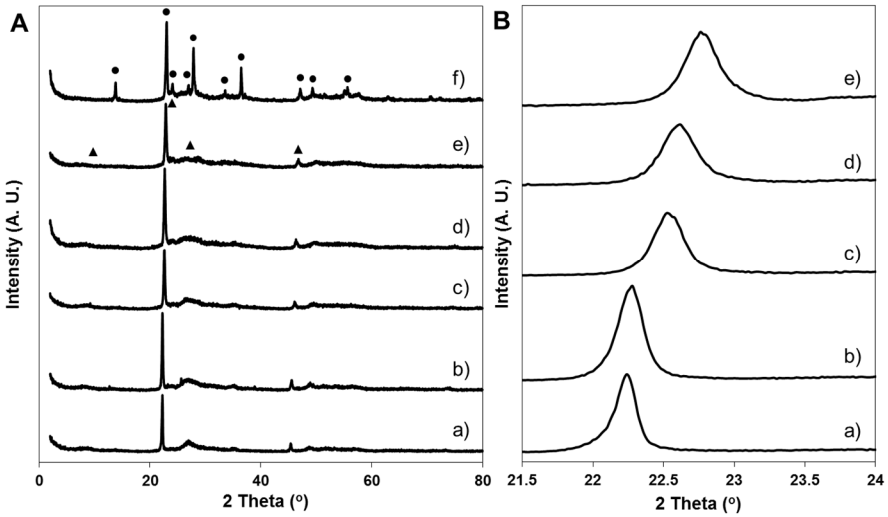

Figure 2-6. A) XRD patterns of a) MoV, b) MoVW-1, c) MoVW-3, d) MoVW-5, e) MoVW-7, and f) MoVW-9 catalysts. B) Effect of the amount of tungsten atoms on the shift in XRD patterns. ●: hexagonal tungsten bronze ▲: amorphous MoV.

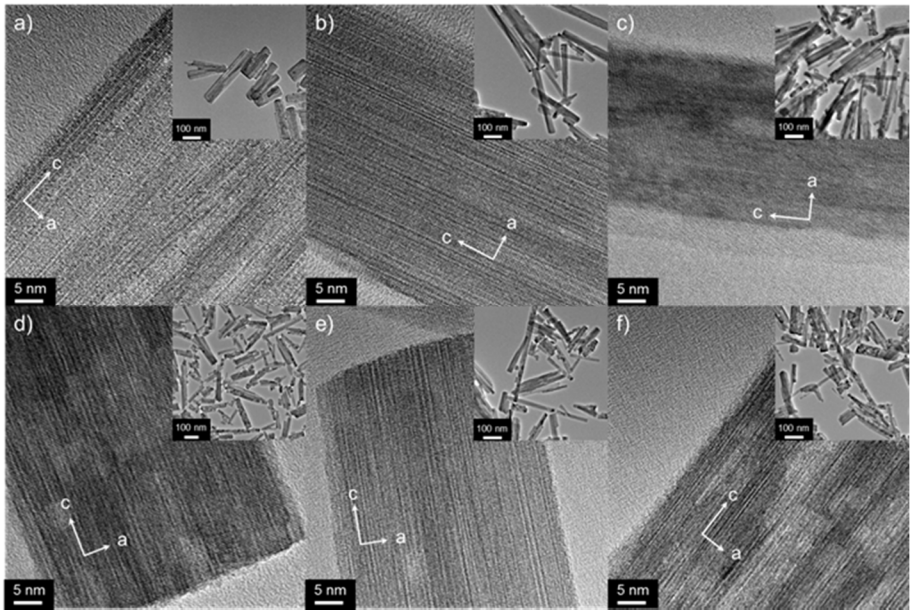

Figure 2-7. HR-TEM images of a) MoV, b) MoVW-1, c) MoVW-3, d) MoVW-5, e) MoVW-7, and f) MoVW-9 catalysts. Insets indicate low magnification images.

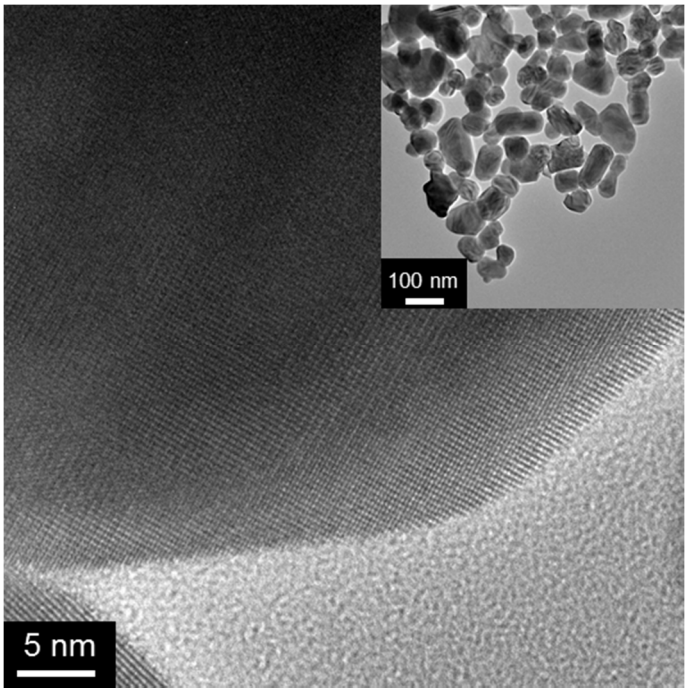

Figure 2-8. TEM images of the WO_3 catalyst prepared by a hydrothermal method.

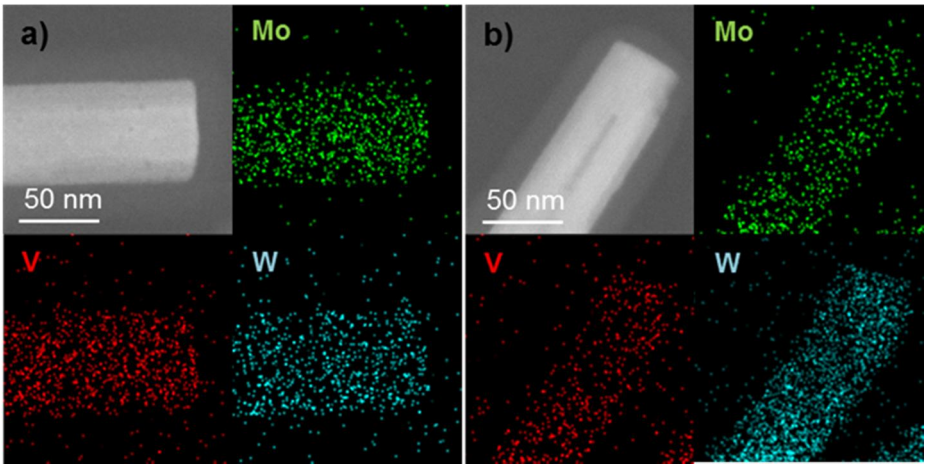

Figure 2-9. HAADF-STEM images of a) MoVW-1, b) MoVW-5, and their corresponding elemental mapping images of Mo (green), V (red), and W (sky blue).

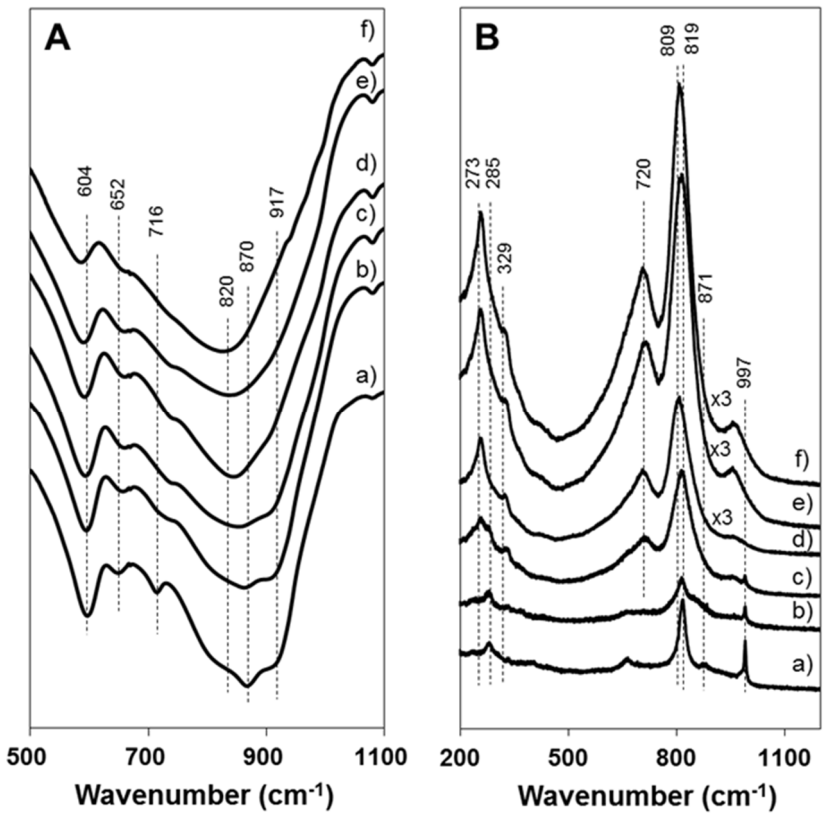

Figure 2-10. (A) FT-IR and (B) Raman spectra of a) MoV, b) MoVW-1, c) MoVW-3, d) MoVW-5, e) MoVW-7, and f) MoVW-9 catalysts.

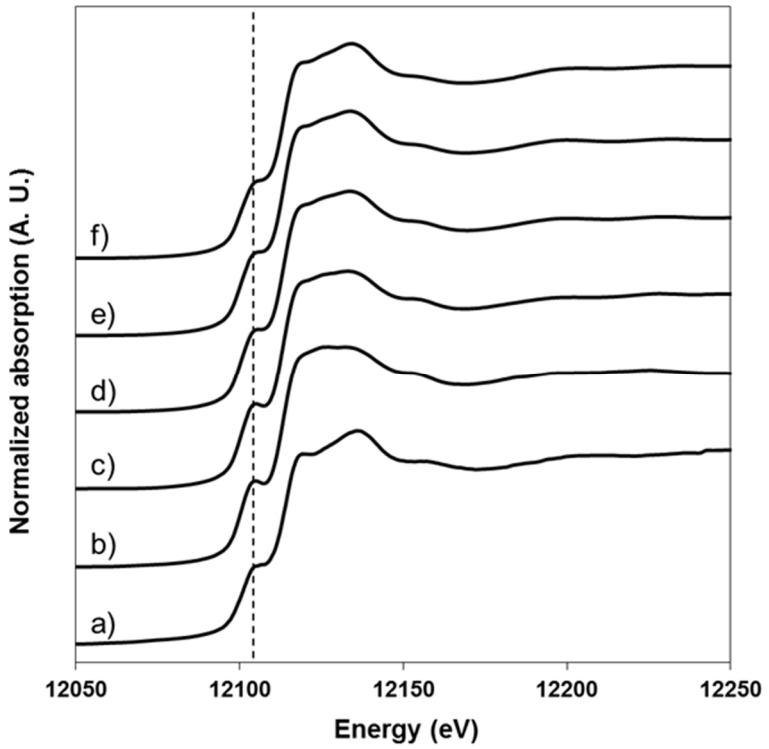

Figure 2-11. W L_1-edge XANES spectra of a) WO_3, b) MoVW-1, c) MoVW-3, d) MoVW-5, e) MoVW-7, and f) MoVW-9 catalysts.

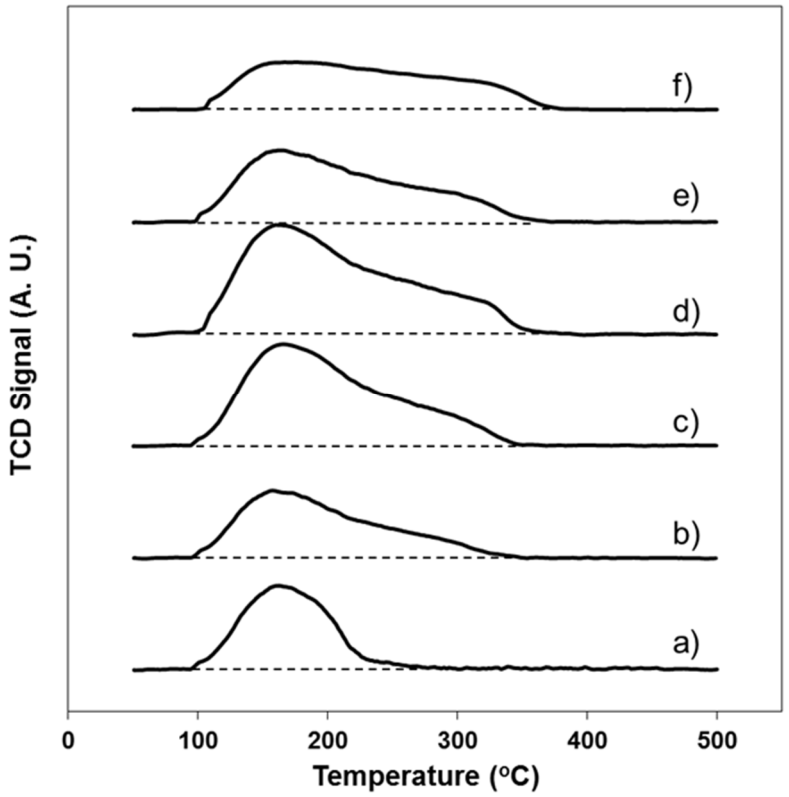

Figure 2-12. NH_3-TPD curves of a) MoV, b) MoVW-1, c) MoVW-3, d) MoVW-5, e) MoVW-7, and f) MoVW-9 catalysts.

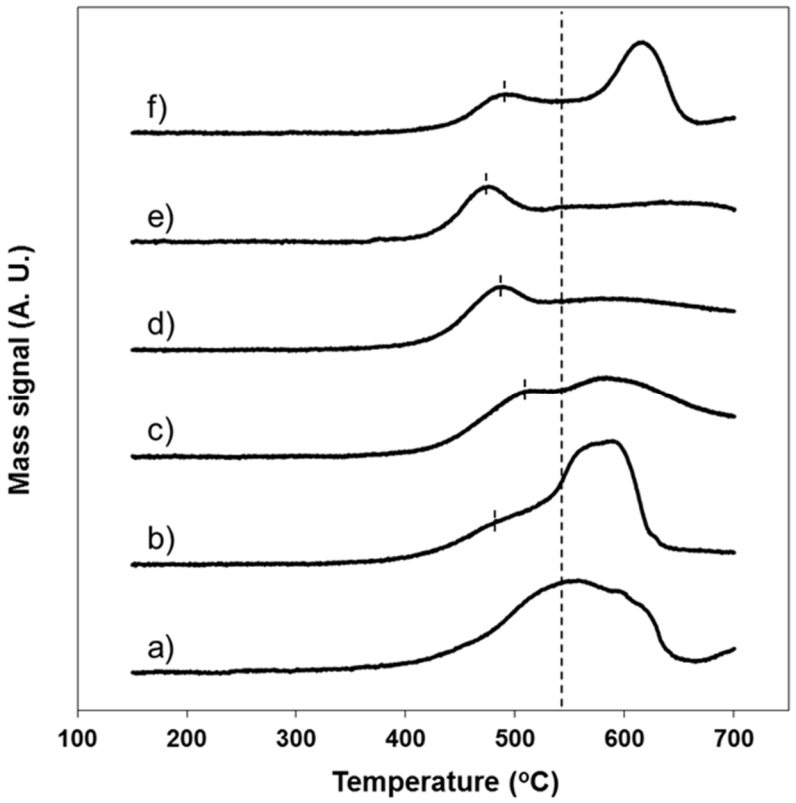

Figure 2-13. H_2-TPR curves of a) MoV, b) MoVW-1, c) MoVW-3, d) MoVW-5, e) MoVW-7, and f) MoVW-9 catalysts.

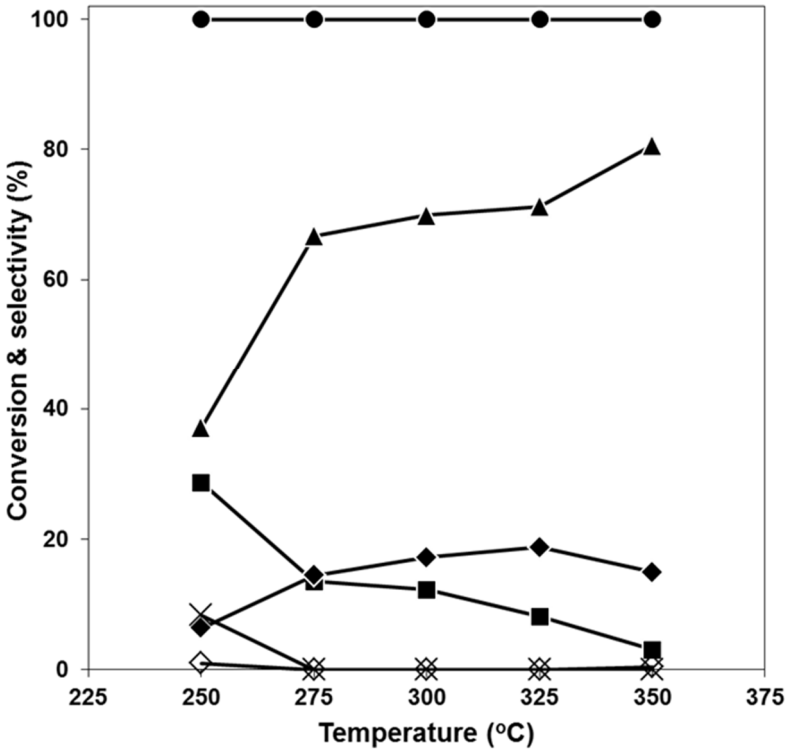

Figure 2-14. Glycerol conversion (●) and product selectivities (▲: CO + CO_2, ■: Acrylic acid, ◆: Acetic acid, X: Acrolein and ◇: Acetaldehyde) in oxydehydration of glycerol over MoVW-5 catalyst as function of reaction temperature. Reaction condition: catalyst amount 0.3 g; total feed rate 74.34 mL min^{-1}; feed composition (vol.%) glycerol/O_2/H_2O/N_2/He=1.3/2.6/55.1/37.0/3.9. The reaction results were taken after 3 h time-on-stream.

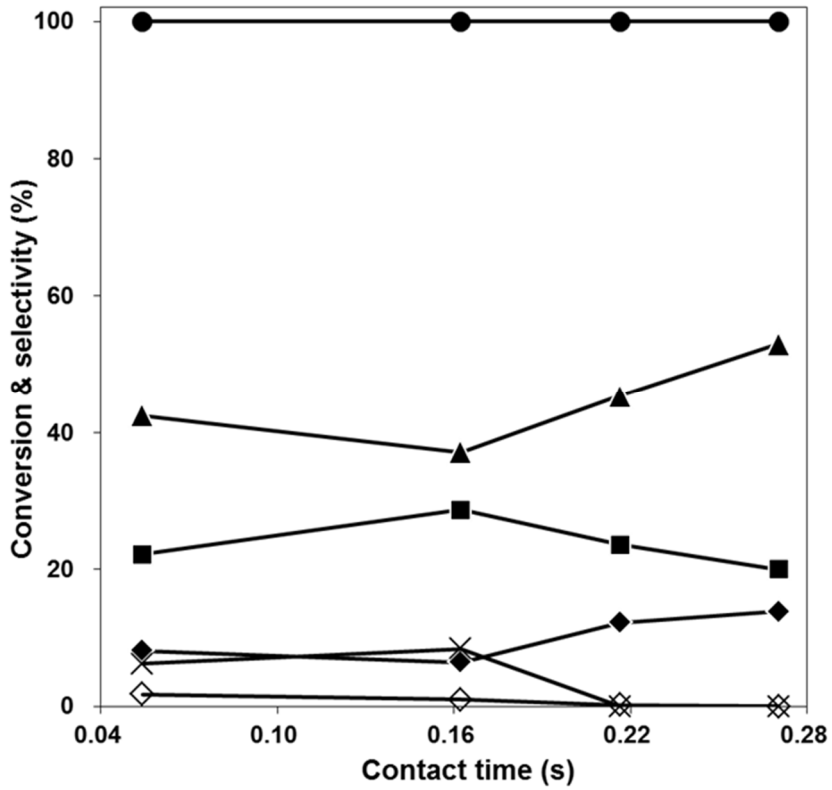

Figure 2-15. Glycerol conversion (●) and product selectivities (▲: CO + CO_2, ■: Acrylic acid, ◆: Acetic acid, X: Acrolein and ◇: Acetaldehyde) in oxydehydration of glycerol over MoVW-5 catalyst as function of contact time. Reaction condition: reaction temperature 250 ^{o}C; total feed rate 74.34 mL min^{-1}; feed composition (vol.%) glycerol/O_2/H_2O/N_2/He=1.3/2.6/55.1/37.0/3.9. The reaction results were taken after 3 h time-on-stream.

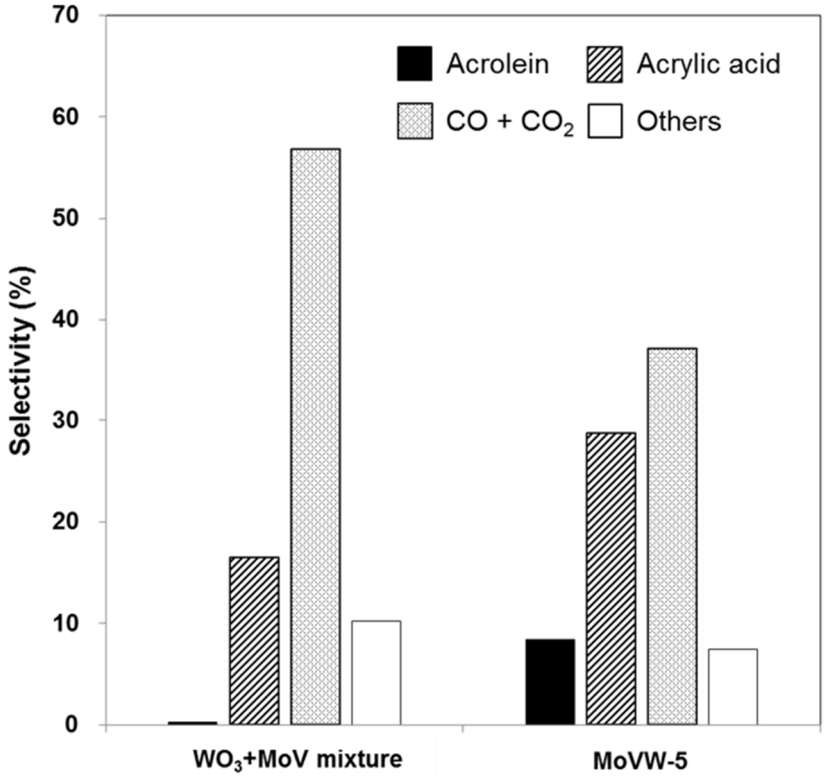

Figure 2-16. Comparative study of physically mixed WO_3 and MoV catalysts, and MoVW-5 catalyst in oxydehydration of glycerol. Reaction condition: MoVW-5 0.3 g; reaction temperature 250 ^oC; total feed rate 74.34 mL min^{-1}; feed composition (vol.%) glycerol/O_2/H_2O/N_2/He=1.3/2.6/55.1/37.0/3.9. The reaction results were taken after 3 h time-on-stream. Mixed system: WO_3 0.1646 g, MoV 0.135 g. Others include acetaldehyde and acetic acid.

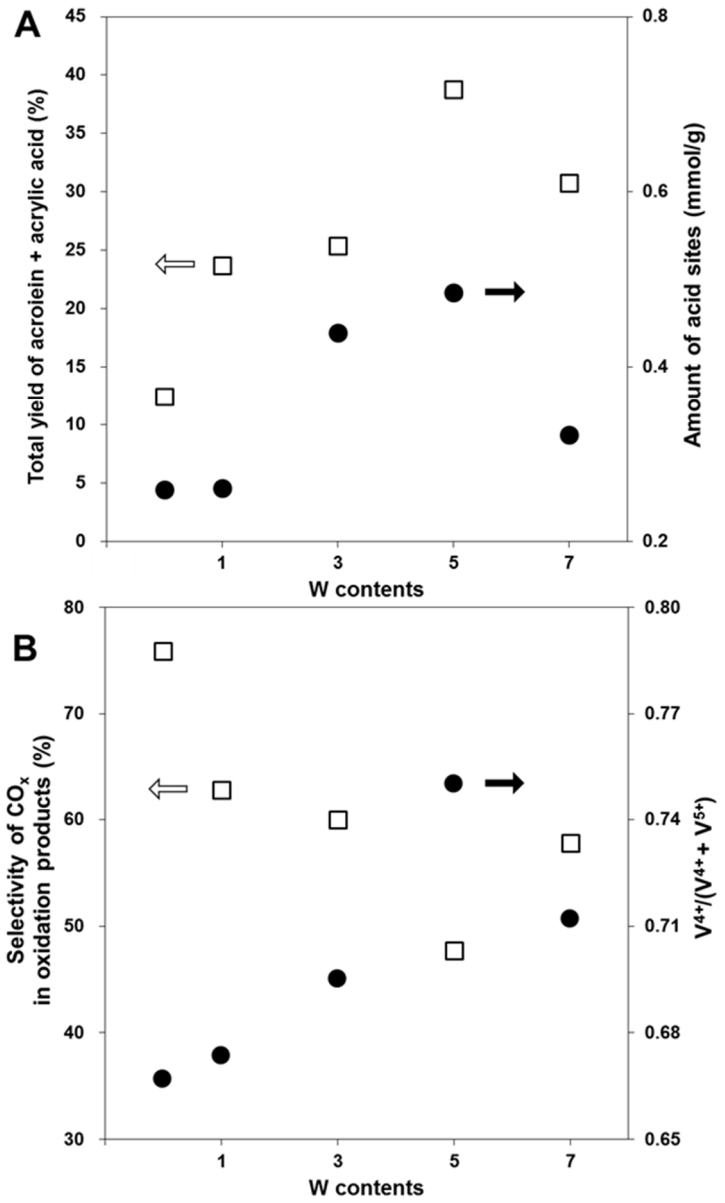

Figure 2-17. Correlations of (A) total yield of acrolein and acrylic acid with amount of acid sites, and (B) selectivity of CO and CO_2 in oxidization products with surface ratio of $V^{4+}/(V^{4+}+V^{5+})$ as function of tungsten contents.

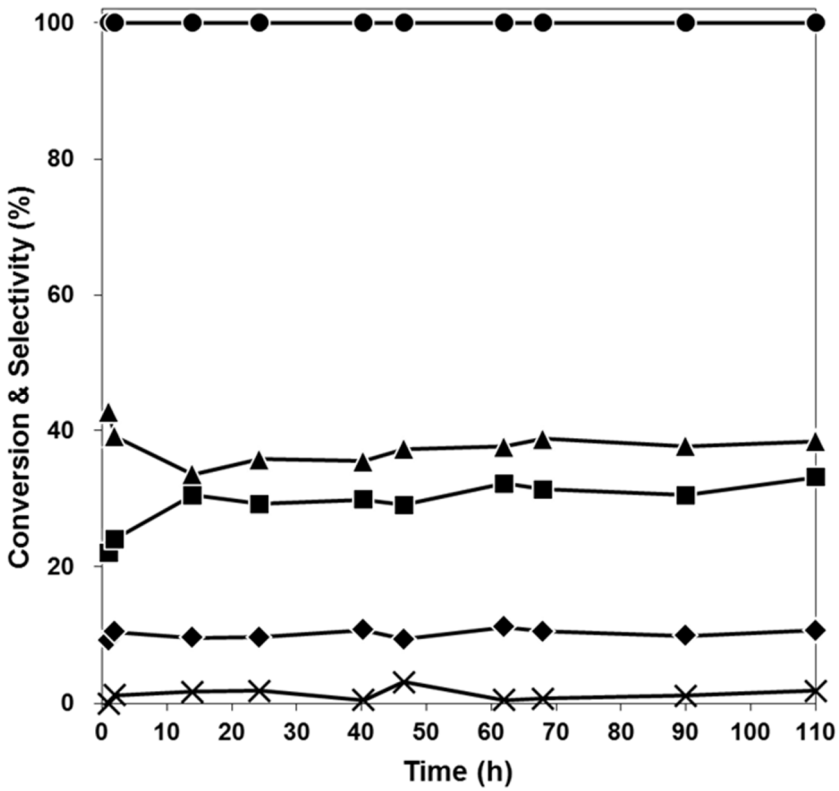

Figure 2-18. Long-term test of MoVW-5 in oxydehydration of glycerol: Glycerol conversion (●) and product selectivities (▲: CO + CO_2, ■: Acrylic acid, X: Acrolein, and ◆: Others). Reaction condition: catalyst amount 0.3 g; reaction temperature 250 ^{o}C; total feed rate 74.34 mL min^{-1}; feed composition (vol.%) glycerol/O_2/H_2O/N_2/He=1.3/2.6/55.1/37.0/3.9. Others include acetaldehyde and acetic acid.

Chapter 3. Control of catalytic reactivity for carbon monoxide hydrogenation by tuning electronic state via doping method

3.1 Introduction

High activity and selectivity in heterogeneous catalysis are highly desirable for sustainable chemical processes [54,85,86]. Many researchers have attempted to develop efficient catalyst for specific reaction. For example, they combined several active components, changed structure of catalyst to control accessibility of reactant and product to active site, grafted additional functionality on the catalyst surface, controlled size of metal particle, and so on [87-89]. As a result, suitable catalysts have been reported and used in industrial field for chemical production. Despite their success in the aspect of performance, there is still lack of fundamental understanding for catalytic activity and selectivity [90-92]. So, it impedes a rational design of catalyst.

Electronic structure of a catalyst is critical factor to determine catalytic performance in photo-catalysis whereas it is less considered in catalysis of chemical conversion [93-95]. Recently, some interpretations of catalytic performance based on electronic structure have been reported [54,96,97]. However, they are still at an early stage.

Herein, we report a strategy to tune catalytic activity of nanoparticles

supported on graphene by controlling the electronic state of the active metal. For the variation in electronic state of the catalyst, hetero-atoms (N or B) were introduced to graphene with various concentrations. Then, active metal was loaded on the doped graphene, inducing to change in electronic state of active metal. The variation in electronic state of active metal was confirmed by experimental characterizations and theoretical calculations. It was noteworthy that the catalytic activity of CO hydrogenation was controlled toward not only enhancement but also decline. Kinetic study and theoretical calculations revealed that change in interactions between active metal and reactant by controlling electronic state affected catalytic activity. It was proven that the strategy can be applied to not only transition metal but also noble metal in other model reactions (4-nitrophenol reduction and benzene hydrogenation as well as CO hydrogenation).

3.2 Experimental

3.2.1 Preparation of catalysts

Grahpene oxide (GO) was prepared by the the improved method, following a procedure reported in the previous literature [98]. 1.5 g of Graphite flakes (Sigma–Aldrich) was added to amixture of 180 ml of concentrated H_2SO_4 (≥95%, Samchun) and 20 mL of H_3PO_4 (≥85%, Samchun), and 9.0 g of KMnO4 (99%, Sigma–Aldrich) was then slowly added with vigorous stirring for 12 h at 40 ◦C. The mixture was cooled to room temperature, and 200 mL of a H_2O_2 solution (190 mL of deionized water + 10 mL of 30 wt% H_2O_2) was then added. The solution stirred for 1 h. The resultant solution was centrifuged. The pre-cipitate was then washed with deionized water water, HCl (35-37%, Samchun), and ethanol repeatedly. The washed precipitate was coagulated with ether (≥99%, Sigma–Aldrich). Finally, yellow powder was obtained by vacuum-drying overnight at room temperature.

For the preparation of nitrogen-doped graphene (NGra), the 2 g of GO was heated under ammonia atmosphere at different temperatures (700, 800, and 900 ^oC) for 4 h. The as-obtained samples are denoted herein as NGra-7, NGra-8, and NGra-9. Boron-doped graphene (BGra) was syntehsized by annealing 2 g of GO powder with mixed with excess boric acid under N_2 atmosphere at different temperatures (700, 800, and 900 ^oC) for 4 h. The as-obtained samples are denoted as BGra-7, BGra-8, and BGra-9. Undoped-graphene (Gra) was prepared by annealing 2 g of GO powder under N_2

atmosphere at 500 ^{o}C for 4 h.

3 wt.% cobalt supported on NGra, BGra, and Gra (Co/NGra, Co/BGra, and Co/Gra) was prepared by following procedure. 0.3 g of support (NGra, BGra, or Gra) was dispersed in admixture of 15 mL of ethanol (≥99.5, Sigma-Aldrich) and 15 mL of deionized water, and sonicated for 1 h. Then, 1mL of aqueous solution containing calculated amount of cobalt nitrate hexahydrate (99.999%, Sigma-Aldrich) was added to the support dispersed solution. Further sonication was introduced for 1 h. The solvent was then removed by evaporation under reduced pressure at room temperature, and the resulting solids were dried overnight at 80 ^{o}C. The samples were reduced in a stream of 10 vol.% of H_2/He at 550 ^{o}C for 3 h. 3 wt.% nickel supported on NGra-7, BGra-7, and Gra, denoted as Ni/NGra-7, Ni/Gra, and Ni/BGra-7, were prepared with the same procedure to that of Co/NGra, Co/BGra, and Co/Gra.

Cube-shaped palladium nanoparticles were synthesized according to a previously decribed method [99]. In a typical synthesis, 8.0 mL of an aqueous solution containing 0.105 g of poly(vinyl pyrrolidone) (PVP, MW= 55000, Sigma-Aldrich), 0.06 g of L-ascorbic acid (AA, Sigma-Aldrich), 0.3 g of potassium bromide (KBr, Sigma-Aldrich) was heated in a 50 mL flask for 10 min at 80 ^{o}C with vigorous stirring. Then, 3.0 mL of an aqueous solution of 0.063 g of potassium tetrachloropalladate (II) (Aldrich) 1098844-1g; 63 mg) was added, and the mixture was stirred at 80 ^{o}C for 3 h. The product was collected by centrifugation and washed three times with deionized water. Palladium nanoparticles supported on NGra-7, BGra-7, and Gra were prepared by incipient wetness method. The samples were denoated

as Pd/NGra-7, Pd/BGra-7, and Pd/Gra.

3.2.2 Characterization

XRD patterns of the catalysts were measured by using a Rigaku d-MAX2500-PC powder X-ray diffractometer operating at 50 kV and 100 mA using CuKa radiation (1.5406 Å). High-resolution transmission electron micrograph (HR-TEM) images were obtained on JEOL JEM-3010 microscope with an acceleration voltage of 300 kV. The N_2 physisorption were carried out on a Micrometrics ASAP-2010 system. The total surface area of the samples was calculated by the BET method (P/P_o=0.05~0.15). Raman spectroscopy was performed on a HORIBA T64000 using a multichannel charge-coupled device (CCD) detector at room temperature. The external laser source was used for excitation, an Ar laser at 514 nm. The loading amount of active metal (cobalt) on support was analyzed by inductively coupled plasma atomic emission spectroscopy (ICP-AES, OPTIMA 4300DV). X X-ray photoelectron spectroscopy (XPS) was performed with a Sigma Probe instrument (ThermoVG). The binding energy of each element was calibrated by using the carbon peak as standard (C 1s = 284.5 eV).

3.2.3 Catalytic activity test

The catalytic activity test for CO hydrogenation was carried out at atmospheric pressure at 450 ^{o}C. A 0.1 g of powder sample was loaded into a quartz reactor (11 mm inner diameter), the reactor was then placed in an electric furnace. The temperature of the catalyst bed was monitored by a thermocouple and controlled through a PID controller. Before the reaction, the catalyst was preheated to the reaction temperature under an reducing atmosphere (H_2 and N_2) at 450 ^{o}C for 1 h. Total flow was fixed to 41 mL. The molar ratio of H_2 to CO is 2. N_2 and He were used as an internal standard and a carrier, respectively.

Benzene hydrogenation was carried out using 0.2 g of catalyst, 30 mL of benzene (Samchun) at 160 ^{o}C with 20 bar of H_2 pressure for 12 h. The conversion of was determined on-line by a gas chromatograph (Younglin, ACME 6100) equipped with a FID detector and a HP-Innowax capillary column.

For 4-nitrophenol (4-NP) reduction, 0.1 mg of catalyst was added to an aqueous solution of 5.618 mM of NaBH4 and 0.112 mM of 4-NP at room temperature. The time dependent reduction was elucidated from the absorbance spectra which were recorded with a Jasco V670 spectrometer.

3.2.3 Computational details

The Vienna Ab-initio Simulation Package (VASP) was employed for density functional theory (DFT) calculations [62]. The exchange-correlation functional was treated within the generalized gradient approximation (GGA) parameterized by the Perdew-Burke-Ernzerhof (PBE) [63]. The electron-ion interaction was described by the projector augmented wave (PAW) method [64]. Dispersion forces were included with the DFT-D2 Grimme's empirical correction [100]. For the bulk optimization of graphene, N-doped graphene (NG), and B-doped graphene (BGra), the wave functions were constructed from the expansion of planewaves with an energy cutoff of 520 eV. A 9 × 9 × 1 Monkhorst-Pack sampling in the Brillouin zone is used for the bulk optimizations. For the other calculations, an energy cutoff of 400 eV was used. A Monkhorst−Pack mesh of 5 × 5 × 1 *k*-points was used for the Brillouin zone. The self-consistent iterations were converged within a criterion of 2×10^{-4} eV, and the ionic optimization steps were converged to 0.03 eV/Å. A Methfessel−Paxton smearing of 0.2 eV and a Gaussian smearing of 0.01 eV were used for the optimized NGra, BGra, and Gra models, and Co/NGra, Co/BGra, and Co/Gra, respectively. Atomic charge analysis was performed using a Bader charge analysis [65].

Charge variation in atom of molecule or slab was calculated as

$$\Delta q = q_{\text{non-interacting}} - q_{\text{interacting}}$$

where $q_{non\text{-}interacting}$ is the charge of the atom in non-interacting system (the bare slab or the molecule in the gas phase), and $q_{interacting}$ is the charge of the atom in the system at which the molecule is adsorbed on the slab. In this convention, negative value indicates a gain of electron.

3.3 Results and discussion

3.3.1 Catalyst characterization

Graphene have drawn attention as versatile supports due to its mechanical, electrical, thermal properties [101-103]. Above all, tunable chemical and electronic properties providing a multitude of design possibilities are most fascinating feature of the material [104-108]. In spite of the inertness of pure carbon materials, modification of the surface can effectively induce changes in the properties of the catalytic systems. In this context, substitutional heteroatom doping of graphene is considered as a promising route to tune electronic features of the graphene support [109,110]. Nitrogen and boron are attractive candidates for this. Nitrogen and boron can have opposite impact on electronic state owing to the difference in the electronegativity compared with carbon [111,112]. Therefore, we use doping method to change electronic state of graphene supporting. Especially, the catalyst system, metal/B-doped carbon materials, has rarely reported before while various N-doped carbon supports have enabled diverse progress.

The prepared samples were examined by transmission electron microscopy (TEM). The well dispersed nanoparticle of cobalt was observed and the corresponding images are shown in Figure 3-1. It is well known that catalytic activity of cobalt nanoparticle for CO hydrogenation depends on the particle size in the small-size range (< 6nm) [113]. According to the previous research, it was reported that the catalytic performance decreases as the

cobalt nanoparticle size is below 6 nm whereas the influence of particle size is negligible when the particle is larger than 6 nm. In this study, the cobalt nanoparticle size of Co/NGra, Co/Gra, and Co/BGra are shown to be above 6 nm. Therefore the particle size can be ruled out of crucial factor for determining catalytic performance among the samples. In XRD patterns (Figure 3-2), it is confirmed that the cobalt species are present in metallic phase, and exhibit similar crystallinity among them. Thus, it is expected that the influence of phase and crystallinity on catalytic activity are excluded.

The physical properties of Co/NGra, Co/Gra, and Co/BGra were characterized by BET and ICP analyses. As shown in Figure 3-3, the isotherms of the catalysts exhibited pseudo type-II pattern, which originated from slit-like open pores [114]. The BET surface area of the catalysts was increased according to the annealing temperature from 700 ^{o}C to 900 ^{o}C in the both cases of N and B doped-graphenes. Similar loading amount (3 wt.%) of cobalt was confirmed regardless of supports (Table 3-1).

To investigate the electronic state of NGra, BGra, Gra and active metal (cobalt), XPS analysis was carried out for the samples. The N1s spectra (Figure 3-4) can be deconvoluted into the different types of nitrogen, which are pyridinic/N-Co (398.1 eV), pyrrolic (399.5 eV), quaternary$_{center}$ (400.9 eV) and quaternary$_{valley}$ (402.5 eV) [115]. For quaternary N, three valence electrons of nitrogen form three σ bonds with the neighboring carbon atoms, one electron is engaged in a π bond formation, and the fifth electron is partially involved in the π*-state of the conduction band. For NGra, as the annealing temperature increases, a decreasing trend for pyrrolic and pyridinic

N, and an increasing trend for quaternary N species (center and valley) were observed. It was previously reported that graphitic N shifted up Fermi level acting as a n-type dopant while pyridinic and pyrrolic N decreased Fermi level acting as a p-type dopant [116]. Therefore, it can be expected that the electron density of NGra is increased as the annealing temperature under NH_3 atmosphere is increased.

The B1s peak for Co/BG-9 also includes three different doping state of boron within graphene, which are BC_3 (190.9 eV), BC_2O (192.3 eV), and BCO_2 (193.2 eV) (Figure 3-5). For BGra, concentration of substitutional doping (BC_3) for B atom into graphene framework was increased as the annealing temperature was increased. Considering that substitutional doping of B atom into graphene is well known as a p-type dopant, downshift Fermi-level of BGra is expected compared to Gra.

By DFT calculations, we also obtained that substitutional doping of N and B atoms leads to upshift and downshift of calculated Fermi level referring to Gra, respectively (Table 3-2). Thus, it was confirmed that electron-rich and -deficient supports were induced by chemical doping method.

To investigate electronic state of active metal, cobalt, XPS analysis was carried out for Co/NGra, Co/Gra, and Co/BGra (Figure 3-6). The Co 2p peak was gradually shifted to lower binding energy from Co/Gra to Co/NGra-9. The opposite shift of Co 2p peak for Co/BGra was obtained referring to Co/Gra. It is noteworthy that the electronic state of active metal was affected by the chemically heteroatoms-doped graphene. The obvious shift of Co 2p peak indicates the Co nanoparticles have a higher electron density for

Co/NGra, and lower electron density for Co/BGra compared to Co/Gra. From the results, it was confirmed that electronic state of active metal was manipulated by facile chemical doping method with variations in type of dopant and concentration.

3.3.2 Reaction test for CO hydrogenation

With the intended modification in electronic structure by hetero-atom doping, catalytic performances of the Co-supported catalysts were evaluated in CO hydrogenation as a model reaction (Figure 3-7). As the obvious differences observed in the position of Co 2p peak above, the differences in the specific activity is even clearer. The specific activity for CO hydrogenation is increased from Co/Gra to Co/NGra-9, exhibiting 7 times higher activity for Co/NGra-9 than Co/Gra. On the other hand, the decreased trend of the specific activity was observed from Co/Gra to Co/BGra-9. Interestingly, in the case of Co/BGra-9, the catalytic activity is almost zero in spite of the negligible differences in properties (size, phase, loading amount of Co etc.) compared with Co/NGra and Co/Gra. We also confirmed that the catalysts without cobalt (NGra, Gra, and BGra) exhibited no catalytic activity. The results implies that the high specific activity is obtained when active metal exhibits high electron density, and vice versa. Therefore, we controlled the catalytic activity by manipulation of electronic state of active metal via facile chemical doping method.

3.3.3 DFT calculations.

To compare the adsorption behavior of CO on Co/NGra, Co/Gra, and Co/BGra, vibrational frequency and charge state of adsorbed CO on the catalysts was calculated by DFT calculations. The calculated vibrational frequency for CO adsorbed on Co/Gra model was determined to be 1727 cm^{-1}. For Co/NGra model, the adsorption band of CO was shifted to a lower frequency than that of Co/Gra. On the other hand, the blue shift was obtained for CO adsorbed on Co/BGra, as compared to the case of CO adsorbed on Co/Gra. The red shift of vibrational frequency corresponding to CO stretch from Co/BGra to Co/NGra is an evidence for the change in the charge state of cobalt [117]. The charge variation of CO molecule comes from degree of back-donation into the antibonding orbital ($2\pi^*$) of CO molecule from cobalt [118,119]. The electron-rich cobalt in Co/NGra facilitates the backdonation, leading to excess of charge in CO molecule and weakening of intramolecular bonds (red shift of vibrational frequency and increases in C-O bond length) compared to Co/Gra. The weakened C-O bond of adsorbed CO molecule on Co/NGra facilitates CO activation, which can result in the ease of CO dissociation assisted by H. The opposite was expected on Co/BGra system. This can explain the variation in catalytic activity among the Co/doped graphene catalysts.

Table 3-1. Elemental analysis of the prepared 3wt.% Co supported on NGra, Gra, and BGra.

	Co content[a] (wt.%)
Co/NGra-9	3.27
Co/NGra-8	2.75
Co/NGra-7	3.41
Co/Gra	4.69
Co/BGra-7	4.04
Co/BGra-8	3.42
Co/BGra-9	3.05

[a]Loading weight percent of Co was analyzed by ICP analysis.

Table 3-2. Calculated Fermi level of NGra, Gra, and BGra models.

	NGra	Gra	BGra
Fermi level	-2.46	-2.76	-3.70

Table 3-3. Calculation results of vibrational frequency (v) for adsorbed CO on Co/NGra, Co/Gra, and Co/BGra models.

Model	v (cm^{-1})
Co/NGra	1660
Co/Gra	1727
Co/BGra	1798

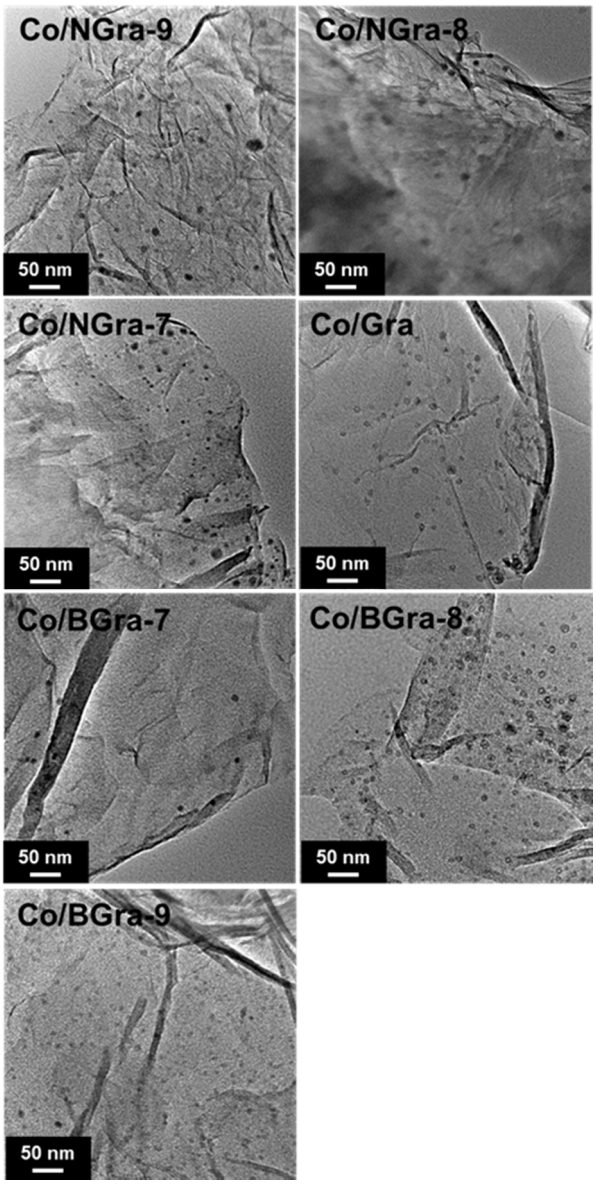

Figure 3-1. TEM images of Co/NGra, Co/BGra, and Co/Gra prepared with different annealing temperatures.

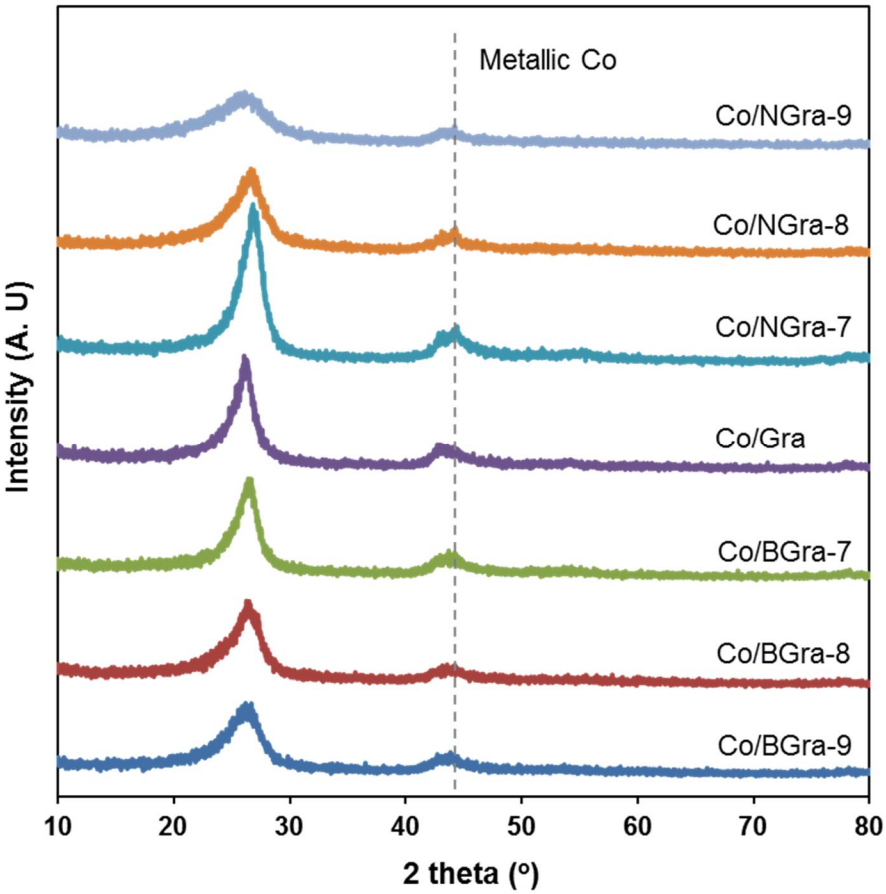

Figure 3-2. XRD patterns of Co/NGra, Co/BGra, and Co/Gra prepared with different annealing temperatures.

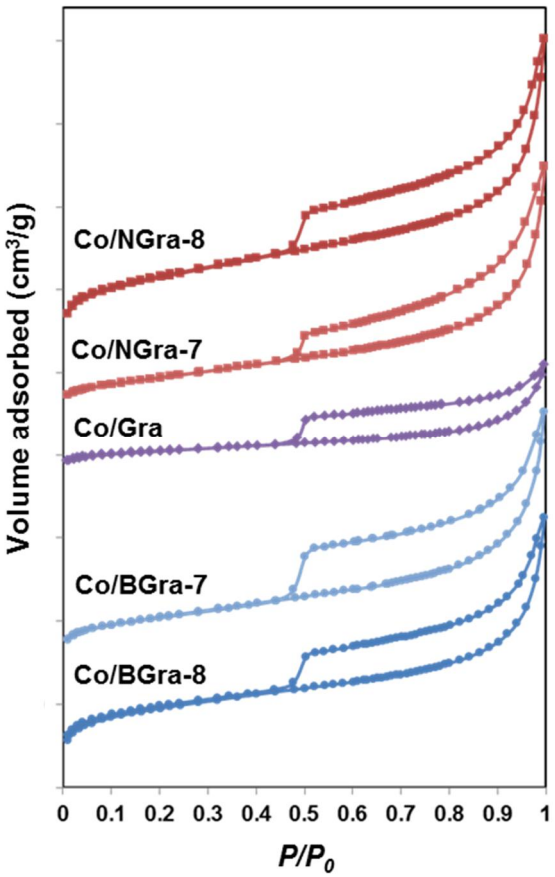

Figure 3-3. N_2 adsorption-desorption isotherms of Co/NGra, Co/BGra, and Co/Gra prepared with different annealing temperatures.

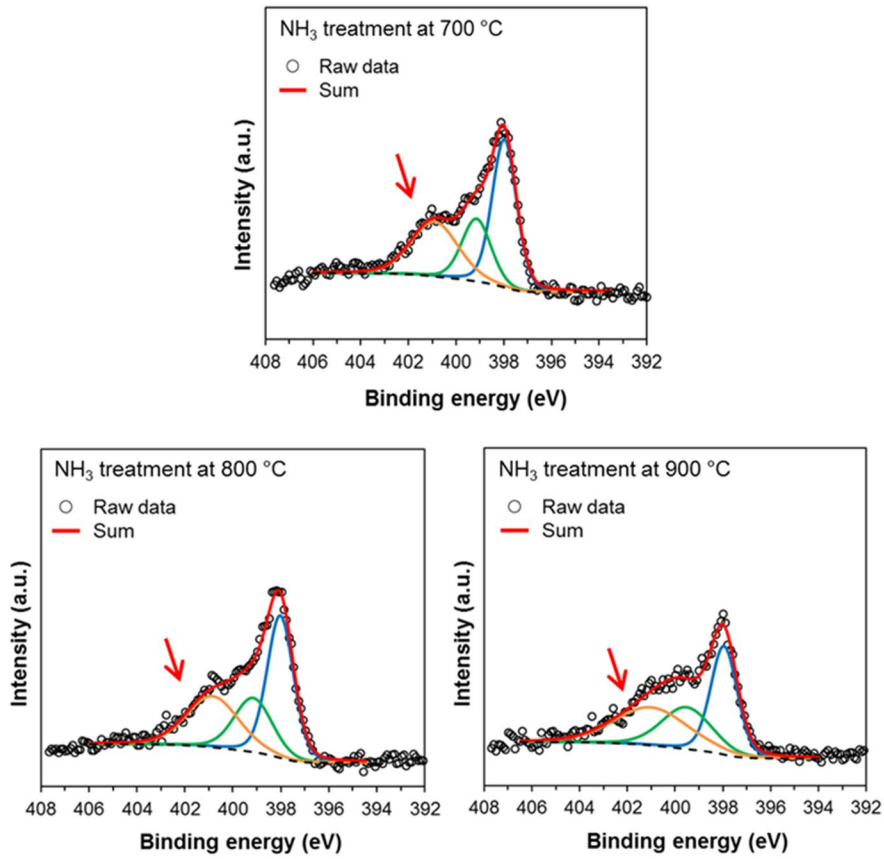

Figure 3-4. N 1s spectra of Co/NGra-7, Co/NGra-8, and Co/NGra-9.

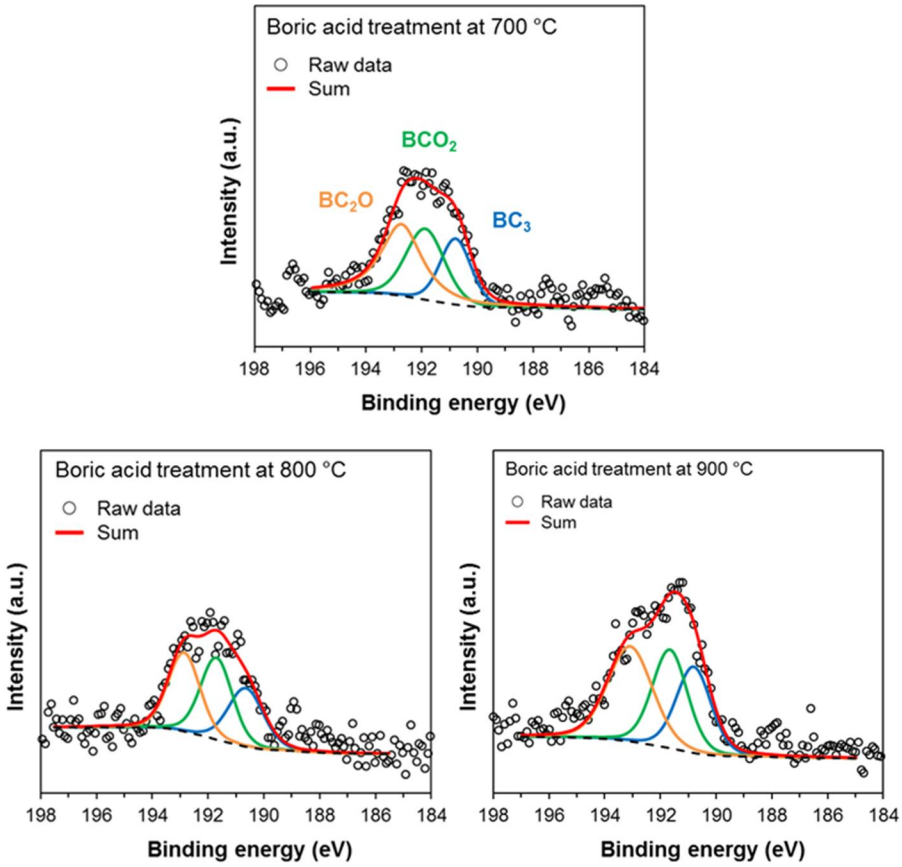

Figure 3-5. B 1s spectra of Co/BGra-7, Co/BGra-8, and Co/BGra-9.

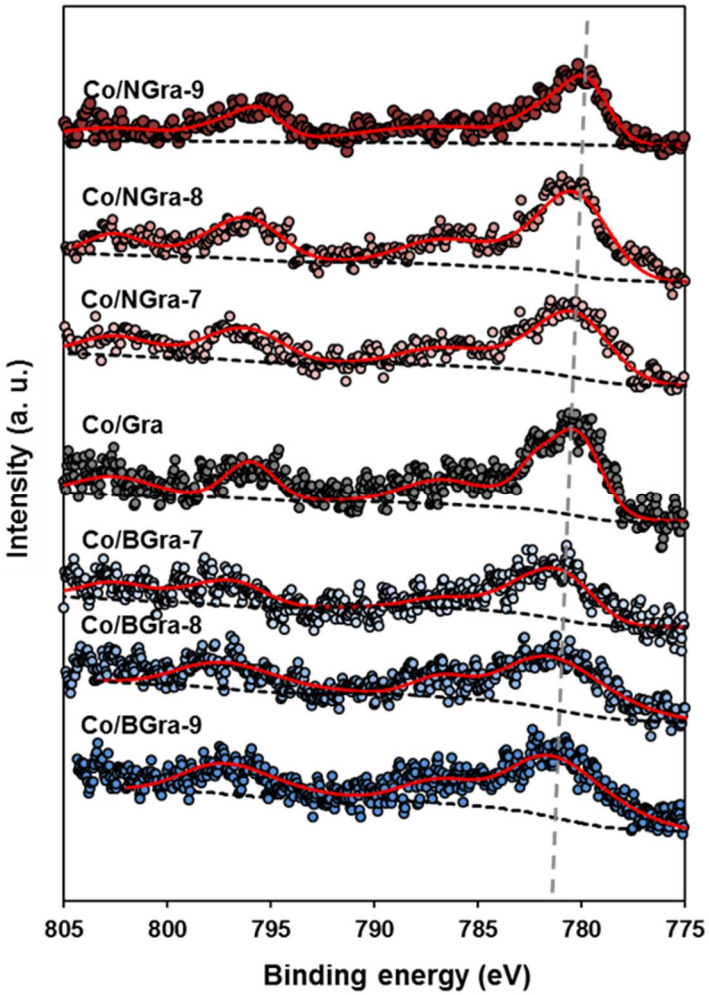

Figure 3-6. XPS spectra of Co 2p for Co/NGra, Co/BGra, and Co/Gra prepared with different annealing temperatures.

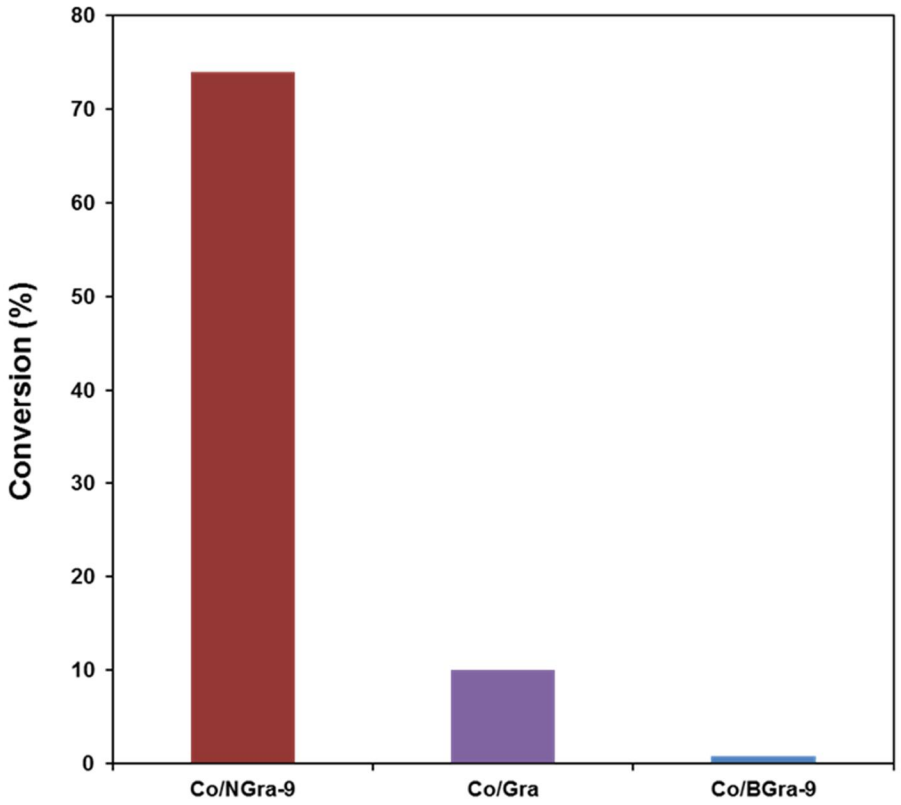

Figure 3-7. Specific activity of CO hydrogenation over 3wt.% Co supported on NGra-9, Gra, and BGra-9 prepared with different annealing temperatures.

Chapter 4. Summary and Conclusions

Using DFT calculations, tungsten incorporated molybdenum vanadium mixed oxide catalysts were designed and used to gain insights into the effect of incorporated tungsten. The findings revealed that incorporated tungsten atoms induce neighboring atoms, such as molybdenum, vanadium, and oxygen, to adopt a reduced state (Mo^{5+} and V^{4+}) and more nucleophilic (oxygen), which are required properties for the selective production of acrylic acid. After confirming this, we successfully prepared the MoVW catalysts with structures similar to the computational models, which was confirmed by experimental characterizations (XRD, XANES, FT-IR, and Raman spectroscopies). XPS studies of the MoVW catalysts were in good agreement with the DFT calculation, demonstrating the validity of the models. NH_3-TPD data indicate that the presence of tungsten in the MoV structure causes an enhancement in both the amount and strength of the acid, thus facilitating dehydration of glycerol to acrolein. The incorporated tungsten species also improve the reducibility of the MoVW catalyst, making the release of lattice oxygen easier. Accordingly, this change in the oxidation state of molybdenum and vanadium, and reducibility promotes the selective and stable conversion of acrolein to acrylic acid. Therefore, the MoVW catalysts exhibit much higher selectivity (MoVW-5; 30.5%) for acrylic acid than the MoV catalyst (12.4%), and a high stability for periods of operation of up to 110 h. The combination of the characterization results with the catalytic reaction results

suggests that a weak-medium acidity and the stabilization of low oxidation state for vanadium induced by the presence of tungsten are main reasons for highly stable production of acrylic acid. A two bed catalytic system including HZSM-5 and MoVW-5 layers exhibited remarkable selectivity (47.2%) for acrylic acid. This report not only shows a high potential for industrial applications of MoVW catalysts but also provides a foundation stone for designing bi-functional catalysts for oxydehydration of glycerol by theoretical studies.

Using doping technique, catalytic activity was successfully controlled according to electronic state of catalyst. Cobalt supported on NGra, BGra, and Gra annealed at different temperature (700, 800, and 900^{o}C) were prepared. The size, phase, and loading amount of active metal were confirmed to be the same among the catalysts by TEM, XRD, ICP analyses. Despite of similarity of physicochemical properties of the catalysts, different catalytic activities for CO hydrogenation were observed over the catalysts. Especially, Co/NGra-9 exhibited 7 times higher than Co/Gra. For Co/BGra, decrease of specific activity was observed compared to Co/Gra. Kinetic studies revealed invariance of the activation energy for CO hydrogenation over the Co/NGra, Co/BGra, and Co/Gra. The difference was found that k_{app} value containing equilibrium constant of hydrogen dissociation. It indicates that Co/NGra catalyst is better activity for utilization of hydrogen than other catalysts. Theoretical calculations showed that C-O bond was weakened in the case of adsorbed CO on Co/NGra and tightened in the case of adsorbed CO on Co/BGra compared to that on Co/Gra. These means that dissociation of CO

adsorbed on Co/NGra assisted by hydrogen can be facilitated, which leads to high catalytic acitivty. The opposite catalytic behavior of Co/BGra can also be explained based on the tighten C-O bond and decreasing ability to utilize H_2. In addition to CO hydrogenation, catalytic activity was changed in benzene hydrogenation and 4-NP reduction according to electronic state of catalysts.

Bibliography

[1] M. Crespo-Quesada, F. Cárdenas-Lizana, A.-L. Dessimoz, L. Kiwi-Minsker, *ACS Catal.* **2012**, 2, 1773-1786.

[2] T. Okuhara, *Chem. Rev.* **2002**, 102, 3641-3666.

[3] F. Su, Y. Guo, *Green Chem.* **2014**, 16, 2934-2957.

[4] D.M. Alonso, S.Q. Bond, J.A. Dumesic, *Green. Chem.* **2010**, 12, 1493-1513.

[5] B. Smith, H.C. Greenwell, A. Whiting, *Energy Env. Sci.* **2009**, 2, 262-271.

[6] P. Kuchonthara, B. Puttasawat, P. Piumsomboon, L. Mekasut, T. Vitidsant, *Korean J. Chem. Eng.* **2012**, 29, 1525-1530.

[7] D.S. Park, D. Yun, T.Y. Kim, J. Baek, Y. S. Yun, Yi, J. *ChemSusChem* **2013**, 6, 2281-2289.

[8] A. Kumar, V. Ramani, *ACS Catal.* **2014**, 4(5), 1516-1525

[9] Z. Huang, F. Cui, H. Kang, J. Chen, X. Zhang, C. Xia, *Chem. Mater.* **2008**, 20, 5090-5099.

[10] H. Yoshida, Y. Yazawa, T. Hattori, *Catal. Today* **2003**, 87, 19-28.

[11] E.W. McFarland, H. Metiiu, *Chem. Rev.* **2013**, 113, 4391-4427.

[12] H.J. Yun, H. Lee, J.B. Joo, N.D. Kim, M.Y. Kang, J. Yi, *Appl. Catal. B* **2010**, 94, 241-247.

[13] S. Agnoli, M. Favaro, *J. Mater. Chem. A*. **2016**, 4, 5002-5025.

[14] A. Witsuthammakul, T. Sooknoi, *Appl. Catal. A* **2012**, 413-414, 109-116.

[15] X. Feng, B. Sun, Y. Yao, Q. Su, W. Ji, C.-T. Au, *J. Catal.* **2014**, 314, 132-141.

[16] P. Kampe, L. Giebeler, D. Samuelis, J. Kunert, A. Drochner, F. Haaß, A.H. Adams, J. Ott, S. Endres, G. Schimanke, T. Buhrmester, M. Martin, H. Fuess, H. Vogel, *Phys. Chem. Chem. Phys.* **2007**, 9, 3577-3589.

[17] W. Xu, X. Liu, J. Ren, P. Zhang, Y. Wang, Y. Guo, G. Lu, *Catal. Commun.* **2010**, 11, 721-726.

[18] A.N. Thadani, V.H. Rawal, *Org. Lett.* **2002**, 4, 4321-4323.

[19] S. Sithambaram, R. Kumar, Y.-C. Son, S.L. Suib, *J. Catal.* **2008**, 253, 269-277.

[20] G. A. Somorjai, H. Frei and J. Y. Park, *J. Am. Chem. Soc.* **2009**, 131, 16589-16605.

[21] F. Zaera, *J. Phys. Chem. Lett.* **2010**, 1, 621-627.

[22] F. Zaera, Acc. *Chem. Res.* **2009**, 42, 1152-1160.

[23] Y. Choi, H. Park, Y. S. Yun, J. Yi, *ChemSusChem* **2015**, 8, 974-979.

[24] R.M. Rioux, H. Song, J.D. Hoefelmeyer, P. Yang, G.A. Somorjai, *J. Phys. Chem. B* **2005**, 109, 2192-2202.

[25] S.I. Cho, S.D. Choi, J.-H. Kim, G.-J. Kim, *Adv. Funct. Mater.* **2004**, 14, 49-54.

[26] Y. Choi, Y. S. Yun, H. Park, D. S. Park, D. Yun, J. Yi, *Chem. Commun.* **2014**, 57, 7652-7655.

[27] S. Shan, V. Petkov, L. Yang, J. Luo, P. Joseph, D. Mayzel, B. Prasai, L. Wang, M. Engelhard, C.-J. Zhong, *J. Am. Chem. Soc.* **2014**, 136, 7140-7151.

[28] S. Xie, S.-I. Choi, N. Lu, L.T. Roling, J.A. Herron, L. Zhang, J. Park, J. Wang, Moon.J. Kim, Z. Xie, M. Mavrikakis, Y. Xia, *Nano Lett.* **2014**, 14, 3570-3576.

[29] H. Zhang, L. Lu, K. Kawashima, M. Okumura, M. Haruta, N. Toshima, *Adv. Mater.* **2015**, 27, 1383-1388.

[30] V. Subramania, E.E. Wolf, P.V. Kamat, *J. Am. Chem. Soc.* **2004**, 126, 4943-4950.

[31] S. Zhang, X. Zhang, G. Jiang, H. Zhu, S. Guo, D. Su, G. Lu, S. Sun, *J. Am. Chem. Soc.* **2014**, 136, 7734−7739.

[32] L. Giebeler, A. Wirth, J.A. Martens, H. Vogel, H. Fuess, *Appl. Catal. A* **2010**, 379, 155-165.

[33] M. Sadakane, K. Endo, K. Kodato, S. Ishikawa, T. Murayama, W. Ueda, *Eur. J. Inorg. Chem.* **2013**, 1731-1736.

[34] S.-H. Chai, H.-P. Wang, Y. Liang, B.-Q. Xu, *Green. Chem.* **2007**, 9, 1130-1136.

[35] P. Mars, D.W. van Krevelen, *Chem. Eng. Sci.* **1954**, 3, 41-59.

[36] A.B. Anderson, D.W. Ewing, Y. Kim, R.K. Graselli, J.D. Durrington, J.F. Brazdil, *J. Catal.* **1985**, 96, 222-233.

[37] T.V. Andrushkevich, G.Y. Popova, *Russian Chem. Rev.* **1991**, 60, 1023-1034.

[38] J.B. Wagner, D.S. Su, S.A. Schunk, H. Hibst, J. Petzoldt, R. Schlögl, *J. Catal.* **2004**, 224, 28-35.

[39] U.S. Ozka, R.B. Watson, *Catal. Today* **2005**, 100, 101-114.

[40] J. Tichý, *Appl. Catal. A* **1997**, 157, 363-385.

[41] F. Wang, J.-L. Dubois, W. Ueda, *J. Catal.* **2009**, 268, 260-267.

[42] J. Deleplanque, J.-L. Dubois, J.-F. Devaux, W. Ueda, *Catal. Today* **2010**, 157, 351-358.

[43] M.D. Soriano, P. Concepción, J.M.L. Nieto, F. Cavani, S. Guidetti, C. Trevisanut, *Green Chem.* **2011**, 13, 2954-2962.

[44] A. Chieregato, F. Basile, P. Concepción, S. Guidetti, G. Liosi, M.D. Soriano, C. Trevisanut, F. Canani, J.M.L. Nieto, *Catal. Today* **2012**, 197, 58-65.

[45] C.F.M. Pestana, A.C.O. Guerra, G. B. Ferreira, C.C. Turci, C.J.A. Mota, *J. Braz. Chem. Soc.* **2013**, 24, 100-105.

[46] K. Omata, K. Matsumoto, T. Murayama, W. Ueda, *Chem. Lett.* **2014**, 43, 435-437.

[47] K. Huang, X.-L. Zhan, F.-Q. Chen, D.-W. Lü, *Chem. Eng. Sci.* **2003**, 58, 81-87.

[48] A.D. Mayernick, M.J. Janik, *J. Catal.* **2011**, 278, 16-25.

[49] M. Kaukonen, A.V. Krasheninnikov, E. Kauppinen, R.M. Nieminen, *ACS Catal.* **2013**, 3, 159-165.

[50] D. Yun, T.Y. Kim, D.S. Park, Y.S. Yun, J.W. Han, J. Yi, *ChemSusChem* **2014**, 7, 2193-2201.

[51] J. Greeley, T.F. Jaramillo, J. Bonde, I. Chorkendorff, J.K. Nørskov, *Nat. Mater.* **2006**, 5, 909-913.

[52] F. Studt, I. Sharafutdinov, F. Abild-Pedersen, C.F. Elkjær, J.S. Hummelshøj, S. Dahl, I. Chorkendorff, J.K. Nørskov, *Nat. Chem.* **2014**, 6, 320-324.

[53] F. Studt, F. Abild-Pedersen, Q. Wu, A.D. Jensen, B. Temel, J.-D. Grunwaldt, J.K. Nørskov, *J. Catal.* **2012**, 293, 51-60.

[54] J.K. Nørskov, T. Bligaard, J. Rossmeisl, C.H. Christensen, *Nat. Chem.* **2009**, 1, 37-46.

[55] A. Ulgen, W. Hoelderich, *Catal. Lett.* **2009**, 131, 122-128.

[56] M. Sadakane, N. Watanabe, T. Katou, Y. Nodasaka, W. Ueda, *Angew. Chem.* **2007**, 119, 1515-1518.

[57] B. Ravel, M. Newville, *J. Synchrotron Rad.* **2005**, 12, 537-541.

[58] R. Häggblad, J.B. Wagner, B. Deniau, J.-M.M. Millet, J. Holmberg, R.K. Grasselli, S. Hansen, A. Andersson, *Top. Catal.* **2008**, 50, 52-65.

[59] Y. Xu, W. Huang, Q. Shi, Y. Zhang, L. Song, Y. Zhang, *J. Sol-Gel Sci. Technol.* **2012**, 64, 493-499.

[60] F. Jing, B. Katryniok, F. Dumeignil, E. Bordes-Richard, S. Paul, *J. Catal.* **2014**, 309, 121-135.

[61] M.A. Cortés-Jácome, C. Angele-Chavez, E. López-Salinas, J. Navarrete, P. Toribio, J.A. Toledo, *Appl. Catal. A* **2007**, 318, 178-189.

[62] G. Kresse, J. Furthmuller, *Phys. Rev. B* **1996**, 54, 11169-11186.

[63] J.P. Perdew, K. Burke, M. Ernzerhof, *Phys. Rev. Lett.* **1996**, 77, 3865-3868.

[64] P.E. Blöchl, *Phys. Rev. B* **1994**, 50, 17953-17979.

[65] R.F.W. Bader, Atoms in Molecules: A Quantum Theory, Oxford University Press, Oxford, 1990.

[66] W. Liu, S. Xu, C. Li, G. Yuan, *Diamond. Relat. Mater.* **2012**, 29, 59-62.

[67] J. Kang, A. Hirata, L. Kang, X. Zhang, Y. Hou, L. Chen, C. Li, T. Fujita, K. Akagi, M. Chen, *Angew. Chem.* **2013**, 52, 1664-1667.

[68] L. Shen, H. Yin, A. Wang, X. Lu, C. Zhang, *Chem. Eng. J.* **2014**, 244, 168-177.

[69] A. Drochner, P. Kampe, J. Kunert, J. Ott, H. Vogel, *Appl. Catal. A* **2005**, 289, 74-83.

[70] B. Botar, P. Kögerler, C.L. Hill, *Chem. Commun.* **2005**, 3138-3140.

[71] T. Konya, T. Katou, T. Murayama, S. Ishikawa, M. Sadakane, D. Buttrey, W. Ueda, *Catal. Sci. Technol.* **2013**, 3, 380-387.

[72] T. Katou, D. Vitry, W. Ueda, *Chem. Lett.* **2003**, 32, 1028-1029.

[73] W. Ueda, N.F. Chen, K. Oshihara, *Chem. Commum.* **1999**, 517-518.

[74] D. Vernardou, H. Drosos, E. Spanakis, E. Koudoumas, C. Savvvakis, N. Katsarakis, *J. Mater. Chem.* **2011**, 21, 513-517.

[75] S. Yamazoe, Y. Hitomi, T. Shishido, T. Tanaka, *J. Phys. Chem. C* **2008**, 112, 6869-6879.

[76] K. Chen, A.T. Bell, E. Iglesia, *J. Phys. Chem. B* **2000**, 104, 1292-1299.

[77] J. Kunert, A. Brochner, J. Ott, H. Vogel, H. Fueß, *Appl. Catal. A* **2004**, 269, 53-61.

[78] Y.-H. Yang, Y.Y. Wang, A.-N. Ko, *J. Porous Mater.* **2011**, 18, 735-742.

[79] J. Ke, J.-W. Xiao, W. Zhu, H. Liu, R. Si, Y.-W. Zhang, C.-H. Yan, *J. Am. Chem. Soc.* **2013**, 135, 15191-15200.

[80] K. Ruth, R. Kieffer, R. Burch, *J. Catal.* **1998**, 175, 27-39..

[81] A. Chieregato, M.D. Soriano, F. Basile, G. Liosi, S. Zamora, P. Concepción, F. Cavani, *Appl. Catal. B.* **2014**, 150-151, 37-46.

[82] W. Suprun, M. Lutecki, T. Haber, H. Papp, *J. Mol. Catal. A* **2009**, 309, 71-78.

[83] Y.T. Kim, K.-D. Jung, E.D. Park, *Appl. Catal. A* **2011**, 393, 275-287.

[84] W. Ueda, D. Vitry, T. Katou, *Catal. Today* **2004**, 96, 235-240.

[85] S. Cao, F.F. Tao, Y. Tang, Y. Lia, J. Yu, *Chem. Soc. Rev.* **2016**, 45, 4747-4765.

[86] B. Yang, R. Burch, C. Hardacre, G. Headdock, P. Hu, *ACS Catal.* **2014**, 4, 182-186.

[87] I. Agirrezabal-Telleria, J. Requies, M.B. Gűemez, P.L. Arias, *Appl. Catal. B.* **2012**, 115-116, 169-178.

[88] J. Oh, S. Dash, H. Lee, *Green Chem.* **2011**, 13, 2004-2007.

[89] Y. Liu, L. Zhang, B.G. Willis, W.E. Mustain, *ACS Catal.* **2015**, 5, 1560-1567.

[90] J. Xiao, L. Kou, C.-Y. Yam, T. Frauenheim, B. Yan, *ACS Catal.* **2015**, 5, 7063-7067.

[91] D. Loffreda, C. Michel, . Delbecq, P. Sautet, *J. Catal.* 2013**,** 308, 374-385.

[92] T. Bligaard, *Angew. Chem.* **2009**, 48, 9782-9784.

[93] Q. Li, H. Meng, P. Zhou, Y. Zheng, J. Wang, J. Yu, J. Gong, *ACS Catal.* **2013**, 3, 882-889.

[94] Q. Xiang, J. Yu, M. Jaroniec, *J. Am. Chem. Soc.* **2012**, 134, 6575-6578.

[95] S. Hu, C. Xiang, S. Haussener, A.D. Berger, N.S. Lewis, *Energy Environ. Sci.* **2013**, 6, 2984-2993.

[96] A. Nilsson, L.G.M. Petterson, B. Hammer, T. Bligaard, C.H. Christensen, J.K. Nørskov, *Catal. Lett.* **2005**, 100, 111-114.

[97] V. Stamenkovic, B.S. Mun, K.J.J. Mayrhofer, P.N. Ross, N.M. Markovic, J. Rossmeisl, J. Greeley, J.K. Nørskov, *Angew, Chem.* **2006**, 118, 2963-2967.

[98] D.C. Marcano, D.V. Kosynkin, J.M. Berlin, A. Sinitskii, Z. Sun, A. Slesarev, L.B. Alemany, W. Lu, J.M. Tour, *ACS Nano* **2010**, 4, 4806-4814.

[99] R. Long, K. Mao, M. Gong, S. Zhou, J. Hu, M. Zhi, Y. You, S. Bai, J. Jiang, Q. Zhang, X. Wu, Y. Xiong, *Angew. Chem.* **2014**, 126, 3269-3273.

[100] S. Grimme, *J. Comput. Chem.* **2006**, 27, 1787-1799.

[101] A.K.Geim, K. S. Novoselov, *Nat. Mater.* **2007**, 6, 183-191.

[102] C. Lee, X. Wei, J.W. Kysar, J. Hone, *Science* **2008**, 321, 385-388.

[103] J.H. Seol, I Jo, A.L. Moore, L. Lindsay, Z.H. Aitken, M.T. Pettes, X. Li, R. Huang, D. Broido, N. Mingo, R.S. Ruoff, L. Shi, *Science*, **2010**, 328, 213-216.

[104] W. Zhang, L. Wu, Z. Li, Y. Liu, *RCS Adv.* **2015**, 5, 49521-49533.

[105] M.J. Allen, V.C. Tung, R.B. Kaner, *Chem. Rev.* **2010**, 110, 132-145.

[106] L. He, F. Weniger, H. Neumann, M. Beller, *Angew. Chem.* **2016**, 55, 12582-12594.

[107] C.N.R. Rao, K. Gopalakrishnan, A. Govindaraj, *Nano Today* **2014**, 9, 324-343.

[108] Z.-H. Sheng, H.-Li Gao, W.-J. Bao, F.-B Wang, X.-H. Xia, *J. Mat. Chem.* **2012**, 22, 390-395.

[109] H. Liu, Y. Liu, D. Zhu, *J. Mater. Chem.* **2011**, 21, 3335-3345.

[110] L. Wang, Z. Sofer, P. Šimek, I. Tomandl, M. Pumera, *J. Phy. Chem. C* **2013**, 117, 23251-23257.

[111] F. Villalpando-Paez, A. Zamudio, A.L. Ellas, H. Son, E.B. Barros, S.G. Chou, Y.A. Kim, H. Muramatsu, T. Hayashi, J. Kong, H. Terrones, G. Dresselhaus, M. Endo, M. Terrones, *Chem. Phys. Lett.* **2006**, 424,345-352.

[112] K. McGuire, N. Gothard, P.L. Gai, M.S. Dresselhaus, G. Sumanasekera, A.M. Rao, *Carbon* **2005**, 43, 219-227.

[113] J. P. den Breejen, P.B. Radstake, G.L. Bezemer, J.H. Bitter, V. Frøseth, A. Holmen, K.P. de Jong, *J. Am. Chem. Soc.* **2009**, 131, 7197-7203.

[114] A. Kaniyoor, T.T. Baby, T. Arockiadoss, N. Rajalakshmi, S. Ramaprabhu, *J. Phys. Chem.* C **2011**, 115, 17660–17669.

[115] C.H. Choi, M.W. Chung, H.C. Kwon, S.H. Park, S.I. Woo, J. Mat. Chem. A 2013, 1, 3694-3699.

[116] T. Schiros, D. Nordlund, L. Pálová, D. Prezzi, L. Zhao, K.S. Kim, U. Wurstbauer, C. Gutiérrez, D. Delongchamp, C. Jaye, D. Fischer, H. Ogasawara, L.G.M. Pettersson, D.R.Reichman, P. Kim, M.S. Hybertsen, A.N.Pasupathy, *Nano Lett.* **2012**, 12, 4025-4031.

[117] B. Yoon, H. Häkkinen, U. Landman, A.S. Wörz, J.-M. Antonietti, S. Abbet, K. Judai, U. Heiz, *Science*, **2005**, 307,403-407.

[118] G. Blyholder, *J. Phys. Chem.* **1964**, 68, 2772-2777.

[119] P.S. Bagus, *Surf. Sci.* **1990**, 236, 233-240.

국 문 초 록

석유로부터 연료와 정밀화학물질을 효율적으로 생산 할 수 있는 촉매를 개발하는 것은 학계뿐만 아니라 산업계에서도 중요하다. 바이오매스와 셰일가스 같이 기존 석유를 대체 할 수 있는 새로운 자원 이용의 필요성이 대두됨에 따라 새로운 촉매 시스템 개발이 필요한 실정이다. 다양한 촉매 개발 방법들 중 도핑은 촉매표면특성을 효과적으로 바꿀 수 있다는 점에서 많은 주목을 받고 있다. 본 논문에서는 이원자 도핑을 통하여 바이오매스유래 물질의 고부가가치 화합물로의 전환반응에 사용되는 이원기능촉매 개발 및 촉매전자상태의 변화를 통한 촉매적 반응활성 조절에 관하여 연구하였다.

글리세롤 산화탈수반응은 아크릴산의 경제적가치가 높아짐에 따라 크게 주목 받고 있는 반응이다. 본 연구에서는 몰리브데넘-바나듐 기반의 복합산화물에 텅스텐이 첨가된 촉매를 개발하였다. 텅스텐이 첨가됨에 따라 촉매는 글리세롤의 탈수반응뿐만 아니라, 중간체인 아크롤레인의 부분산화반응에도 활성을 나타내었다. 엑스선을 이용한 구조분석 및 밀도범함수이론 기반 계산을 통하여 텅스텐이 첨가된 멀리브데넘-바나듐 복합산화물 촉매의 구조를 파악하였다. 개발된 촉매에서 텅스텐은 물질의 산특성 및 산화환원 특성을 증진시켰고, 이를 통하여 30.5%의 높은

아크릴산 선택도를 나타내었다. 텅스텐은 또한 몰리브데넘과 바나듐 원자의 산화수를 낮추는 역할을 하였고, 반응 후에도 보다 환원된 산화수를 유지할 수 있게끔 하는 역할을 하였다. 본 촉매에서 110시간동안 글리세롤 전환율 및 아크릴산 선택도가 유지되어 높은 안정성을 증명하였다. 또한 기존 산촉매를 사용한 이중층 반응시스템에서도 47.2%라는 높은 아크릴산 선택도를 보이며, 높은 상용화 가능성을 나타내었다.

불균일계촉매반응에서 도핑방법을 사용하여 촉매의 전자상태에 변화를 주고 이를 통하여 불균일계촉매반응의 활성을 바꾸는 연구를 진행하였다. 금속이 담지된 그래핀촉매의 전자상태를 바꾸기 위하여 다른 종류의 불순물(dopant, 질소 혹은 붕소)를 도핑하였고, 또한 그 농도를 조절하였다. 엑스레이 광전자 분광법을 통하여 활성금속의 전자상태가 변하는 것을 확인하였다. 활성금속의 크기, 상, 그리고 담지량 등과 같이 활성에 영향을 줄 수 있는 요인을 모두 같게 했음에도 불구하고, 촉매별로 일산화탄소의 수소화 반응 활성이 달라지는 것을 확인하였다. 밀도범함수기반의 계산을 통하여 촉매 전자상태 변화가 반응물의 흡착거동에 영향을 주어 촉매 활성에 영향을 미친다는 것을 밝혔다.

주요어: 비균일계 촉매작용, 도핑, 산화탈수반응, 글리세롤,
아크릴산, 전자상태, 그래핀, 수소화반응
학 번: 2011-21052

List of publications

International Publications

International Academic Published Papers (First Author)

1. **Y. S. Yun**, T. Y. Kim, D. Yun, K. R. Lee, J. W. Han*, and J. Yi*, "Understanding the reaction mechanism of glycerol hydrogenolysis over $CuCr_2O_4$ catalyst", *ChemSusChem*, **2016**, DOI: 10.1002/cssc.201601269.

2. **Y. S. Yun**, K. R. Lee, H. Park, T. Y. Kim, D. Yun, J. W. Han, and J. Yi*, "Rational Design of a Bi-functional Catalyst for the Oxydehydration of Glycerol: A Combined Theoretical and Experimental Study", *ACS Catalysis*, **2015**, 5, 82-94.

3. Y. S. Yun[†], D. S. Park[†], and J. Yi*, "Effect of nickel on catalytic behaviour of bimetallic Cu-Ni catalyst supported on mesoporous alumina for the hydrogenolysis of glycerol to 1,2-propanediol", *Catalysis Science & Technology*, **2014**, 4, 3191-3202.

   ([†] Yang Sik Yun and Dae Sung Park contributed equally to this work.)

4. Y. Choi[†], Y. S. Yun[†], H. Park, D. S. Park, D. Yun, and J. Yi*, "A facile approach for preparation of tunable acid nano-catalyst with hierarchically mesoporous structure", *Chemical Communications*, **2014**, 57(50), 7652-7655.

   ([†] Youngbo Choi and Yang Sik Yun contributed equally to this work.)

International Academic Published Papers (Co-author)

1. D. Yun, **Y. S. Yun**, T. Y. Kim, H. Park, J. M. Lee, J. W. Han, and J. Yi*, "Mechanistic Study of Glycerol Dehydration on Brønsted Acidic Amorphous Aluminosilicate", *Journal of Catalysis*, **2016**, 341, 33-43.

2. H. Park, **Y. S. Yun**, T. Y. Kim, K. R. Lee, J. Baek, and J. Yi*, "Kinetics of the

dehydration of glycerol over acid catalysts with an investigation of deactivation mechanism by coke", *Applied Catalysis B: Environmental*, **2015**, 176, 1-10.

3. Y. Choi†, H. Park†, **Y. S. Yun**, and J. Yi*, "Effects of Pore Structures and Acid Properties on the Catalytic Dehydration of Glycerol", *ChemSusChem*, **2015**, 8(6), 974-979.

4. T. Y. Kim†, J. Baek†, C. K. Song, **Y. S. Yun**, D. S. Park, W. Kim, J. W. Han, and J. Yi*, "Gas-phase Dehydration of Vicinal Diols to Epoxides: Dehydrative Epoxidation over a Cs/SiO_2 catalyst", *Journal of Catalysis*, **2015**, 323, 85-99.

5. D. Yun†, T. Y. Kim†, D. S. Park, **Y. S. Yun**, J. W. Han, and J. Yi*, "A Tailored Catalyst for the Sustainable Conversion of Glycerol to Acrolein: Mechanistic Aspect of Sequential Dehydration", *ChemSusChem*, **2014**, 7(8), 2193-2201.

6. D. S. Park†, D. Yun†, T. Y. Kim, J. Baek, **Y. S. Yun**, and J. Yi*, "A Mesoporous Carbon-Supported Pt Nanocatalyst for the Conversion of Lignocellulose to Sugar Alcohols", *ChemSusChem*, **2013**, 6(12), 2281-2289.

7. J. R. Park, B. K. Kwak, D. S. Park, T. Y. Kim, Y. S. Yun, and J. Yi*, "Effect of Acid Type in WOX clusters on The Esterification of Ethanol with Acetic Acid", *Korean Journal of Chemical Engineering*, **2012**, 29(12), 1695-1699.

8. B. K. Kwak, D. S. Park, Y. S. Yun, and J. Yi*, "Preparation and characterization of nanocrystalline CuAl2O4 spinel catalysts by sol-gel method for the hydrogenolysis of glycerol", *Catalysis Communications*, **2012**, 24, 90-95.

Patents

1. 이종협, 박대성, 윤다님, **윤양식**, 박홍석, “금속이 분산된 열린 기공구조를 가지는 탄소 촉매 및 이를 이용한 소르비톨의 생산방법”, 대한민국특허 **등록** 10-1535123 (2015.07.02)
2. 이종협, 최영보, 박홍석, **윤양식**, “3차원의 열린 기공 구조를 갖는 산성 산화물 나노 입자, 그 제조방법 및 상기 나노 입자를 이용하여 글리세롤로

부터 아크롤레인 또는 아크릴산을 제조하는 방법", 대한민국특허 **등록** 10-1504673 (2015.03.16)

3. 이종협, 최영보, **윤양식**, 박홍석, 윤다님, "3차원의 열린 기공 구조를 갖는 알루미노실리케이트 구형 나노 입자, 그 제조방법 및 상기 나노 입자를 이용하여 글리세롤로부터 아크릴산을 제조하는 방법", 대한민국특허 **등록** 10-1337301 (2013.11.29)

International Conferences (First author)

1. **Y. S. Yun**, K. R. Lee, H. Park, T. Y. Kim, D. Yun, J. W. Han, and J. Yi, "Bi-Functional Mo-V-W-O Catalysts for the One-Step Production of Acrylic Acid from Glycerol and Validation Via First Principle Calculations", 24th North American Catalysis Society Meeting, David L. Lawrence Convetion Center, Pittsburgh, Pennsylvania, USA, June. 14-June. 19 (2015)

2. **Y. S. Yun**, T. Y. Kim, D. Yun, H. Park, J. M. Lee, J. W. Han, and J. Yi, "Mechanistic insight of hydrogenolysis of glycerol over Cu-based catalysts via ab initio calculations", The 15th Korea-Japan Symposium on Catalysis, BEXCO and Haeundae Centum Hotel, Busan, Korea, May. 26-May. 28 (2015)

3. **Y. S. Yun**, K. R. Lee, H. Park, Y.-J. Seo, W. G. Kim, J. W. Han, and J. Yi, "Tungsten oxide promoted molybdenum vanadium mixed oxide catalysts for oxydehydration of glycerol", The Korean Society of Clean Technology 2014 Fall Meeting, K hotel, Gyeongju, Korea, Sep. 24-26 (2014)

4. **Y. S. Yun**, Y. Choi, H. Park, D. Yun, D. S. Park, and J. Yi, "Preparation of 3D Open-Porous Acidic Heterogeneous Catalysts for the Chemical Production", 2013 MRS Fall Meeting Program & Exhibit, Boston, Massachusetts, USA, Dec. 1-6 (2013)

5. **Y. S. Yun**, Y. Choi, H. Park, D. Yun, and J. Yi, "Three dimensionally open porous acid catalysts with adjustable acidic properties", The 14th Japan-Korea Symposium on Catalysis, WINC Aichi, Nagoya, Japan, July 1-3 (2013)

International Conferences (Co-author)

1. H. Park, **Y. S. Yun**, D. Yun, T. Y. Kim, K. R. Lee, J. Baek, M. Lee, and J. Yi, "An investigation of deactivation mechanism by coke via kinetics study of the glycerol dehydration over acid catalysts", 16th International Congress on Catalysis, CNCC, Beijing, China, July. 3-July. 8 (2016)

2. T. Y. Kim, J. Baek, C. K. Song, **Y. S. Yun**, D. S. Park, W. Kim, and J. Yi, "Production of 1,3-Butadiene from 2,3-Butanediol Using Cesium Oxide Supported Silica Catalyst", 24th North American Catalysis Society Meeting, David L. Lawrence Convetion Center, Pittsburgh, Pennsylvania, USA, June. 14-June. 19 (2015)

3. D. Yun, T. Y. Kim, **Y. S. Yun**, J. M. Lee, J. W. Han, and J. Yi, "Ab initio study of the surface model of amorphous aluminosilicate", The 15th Korea-Japan Symposium on Catalysis, BEXCO and Haeundae Centum Hotel, Busan, Korea, May. 26-May. 28 (2015)

4. J. Baek, T. Y. Kim, **Y. S. Yun**, and J. Yi, "Heterogeneous Catalytic Conversions of Alcohols/polyols Derived from Biomasses to Fine Chemicals", The 15th Korea-Japan Symposium on Catalysis, BEXCO and Haeundae Centum Hotel, Busan, Korea, May. 26-May. 28 (2015)

5. K. R. Lee, **Y. S. Yun**, H. Park, Y.-J. Seo, W. G. Kim, and J. Yi, "Development of Scale-up Method of Glycerol Conversion to Bench Scale Reaction", The Korean Society of Clean Technology 2014 Fall Meeting, K hotel, Gyeongju, Korea, Sep. 24-26 (2014)

6. H. Park, **Y. S. Yun**, K. R. Lee, and J. Yi, "Dehydration of Glycerol over Hierarchically Mesoporous Acid Catalysis", The Korean Society of Clean Technology 2014 Fall Meeting, K hotel, Gyeongju, Korea, Sep. 24-26 (2014)

7. T. Y. Kim, J. Baek, C. K. Song, **Y. S. Yun**, D. S. Park, and J. Yi, "Density Functional Theory Study on Conversion of Biomass Derived 2,3-Butanediol to 2,3-

Epoxybutane", The Korean Society of Clean Technology 2014 Fall Meeting, K hotel, Gyeongju, Korea, Sep. 24-26 (2014)

8. D. S. Park, D. Yun, **Y. S. Yun**, H. Park, T. Y. Kim, J. Baek, and J. Yi, "Direct conversion of lignocellulose to sugar alcohols over Pt supported on a new 3D mesoporous carbon", 247th American Chemical Society National Meeting & Exposition, Dallas, Texas, USA, Mar. 16-20 (2014)

9. H. Park, Y. Choi, **Y. S. Yun**, and J. Yi, "Oxy-dehydration of biomass-derived glycerol over acidic nanosphere catalysts with hierarchically mesoporous strutures", The 14th Japan-Korea Symposium on Catalysis, WINC Aichi, Nagoya, Japan, July 1-3 (2013)

10. D. S. Park, **Y. S. Yun**, D. Yun, S. Oh, Y. A. Shin, and J. Yi, "The hydrogenolysis of glycerol on CuNi bimetallic catalyst supported on mesoporous alumina", The 14th Japan-Korea Symposium on Catalysis, WINC Aichi, Nagoya, Japan, July 1-3 (2013)

11. H. Park, Y. Choi, **Y. S. Yun**, and J. Yi, "(Oxy)dehydration of glycerol over wrinkled and 3D porous acid nanosphere", The 6th WCU International Symposium on Chemical Convergence for Energy and Environment, Sheraton Hotel, Incheon, Korea, June 17-18 (2013)

12. B. K. Kwak, **Y. S. Yun**, Y. J. Seo, S. H. Choi, and J. Yi, "Effects of Zn added copper chromite catalysts on glycerol hydrogenolysis to 1,2-PDO", 15th International Congress on Catalysis, Munich, Germany, July 1-6 (2012)

13. B. K. Kwak, D. S. Park, **Y. S. Yun**, and J. Yi, "Synthesis of nanocrystalline copper aluminate (CuAl2O4) by sol-gel technique and its application to the to the glycerol hydrogenolysis", Asian Crystallization Technology Symposium-2012, Korea University Seoul, Korea, May 23-25 (2012)

Domestic Conferences

1. 이민재, 김길표, 이윤재, 배성준, 송현돈, 송인규, **윤양식**, 김윤화, 이종협, “탄소 에어로겔의 고분자 기능화를 통한 고분산 백금 나노촉매 개발 및 전기화학적 성능평가”, 한국화학공학회 2016년도 봄 총회 및 학술대회, 부산 BEXCO, 4. 27-29 (2016)
2. 김태용, 백자연, **윤양식**, 박대성, 문원균, 김우영, 한정우, 이종협, “비시널 디올의 탈수반응을 통한 에폭사이드 화합물의 생성 및 이를 통한 바이오 매스 유래 2,3-부탄디올로부터 1,3-부타디엔 생산”, 한국화학공학회 2014년도 가을 총회 및 학술대회, 대전컨벤션센터, 10. 23-24 (2014)
3. 박홍석, **윤양식**, 김길표, 이민재, 송현돈, 서영종, 김왕규, 이중원, 이종협, “산 촉매에서의 글리세롤 탈수반응에 대한 반응속도론적 연구”, 한국화학공학회 2014년도 가을 총회 및 학술대회, 대전컨벤션센터, 10. 23-24 (2014)
4. **윤양식**, 이경록, 박홍석, 김태용, 윤다님, 서영종, 김왕규, 이중원, 한정우, 이종협, “글리세롤의 산화탈수반응을 위한 이원기능촉매 개발 및 적용”, 한국화학공학회 2014년도 가을 총회 및 학술대회, 대전컨벤션센터, 10. 23-24 (2014)
5. 윤다님, 김태용, 박대성, **윤양식**, 이종협, 한정우, 오석일, 신용안, “글리세롤로부터 아크롤레인을 안정적으로 생산하기 위한 맞춤형 촉매 개발”, 한국화학공학회 2014년도 봄 총회 및 학술대회, 창원컨벤션센터, 4. 23-25 (2014)
6. 박홍석, **윤양식**, 이경록, 이종협, “글리세롤의 산화탈수반응을 통한 아크릴산 생산 기술 개발”, 2014년 한국청정기술학회 춘계 학술발표회, 여수경도리조트, 3. 27-28 (2014)
7. **윤양식**, 박홍석, 이경록, 이종협, “글리세롤로부터 프로판다이올 및 바이오 고분자 생산기술 개발”, 2014년 한국청정기술학회 춘계 학술발표회, 여수경도리조트, 3. 27-28 (2014)
8. **윤양식**, 박홍석, 윤다님, 박대성, 김태용, 백자연, 이경록, 이종협, “계층구조를 갖는 나노크기의 고체산촉매 제조 및 응용”, 2014년 한국청정기술학회 춘계 학술발표회, 여수경도리조트, 3. 27-28 (2014)

9. 윤다님, 김태용, 박대성, **윤양식**, 한정우, 이종협, “열린 기공 구조를 갖는 브뢴스테드 산촉매의 제조 및 글리세롤 탈수반응에의 적용”, 2014년 한국청정기술학회 춘계 학술발표회, 여수경도리조트, 3. 27-28 (2014)
10. 박대성, 윤다님, **윤양식**, 김우식, 이종협, “3차원 중형기공 탄소물질의 개발 및 목질계 바이오매스 전환을 통한 당알코올 생산기술에의 응용”, 2014년 한국청정기술학회 춘계 학술발표회, 여수경도리조트, 3. 27-28 (2014)
11. 김태용, 백자연, 송찬경, **윤양식**, 박대성, 한정우, 이종협, “바이오매스 유래물질의 맞춤형 탈수반응을 위한 비시널 디올로부터 에폭사이드 유래물질 생성”, 2014년 한국청정기술학회 춘계 학술발표회, 여수경도리조트, 3. 27-28 (2014)
12. 백자연, 송현돈, 김태용, 박대성, 윤다님, **윤양식**, 박홍석, 이종협, “금 나노입자의 암모니아 보란을 이용한 4-니트로페놀 환원 반응에서의 실시간 전자이동 관찰”, 2013년 한국청정기술학회 추계 학술발표회, 제주 한화리조트, 9. 25-27 (2013)
13. 박홍석, 최영보, **윤양식**, 이종협, “3차원 계층 구조의 다공성 나노 산 촉매를 이용한 글리세롤의 산화탈수반응”, 한국화학공학회 2013년 봄 총회 및 학술대회, 광주 김대중컨벤션센터, 4. 24-26 (2013)
14. **윤양식**, 최영보, 박홍석, 이종협, “글리세롤을 아크릴산으로 직접 전환하기 위한 이원기능촉매의 제조 및 분석”, 한국화학공학회 2013년 봄 총회 및 학술대회, 광주 김대중컨벤션센터, 4. 24-26 (2013)
15. **윤양식**, 박대성, 윤다님, 김태용, 오석일, 이종협, “무수소 조건에서의 글리세롤의 가수소분해 반응을 위한 중형기공 알루미나에 담지된 구리-니켈 이중금속촉매의 제조 및 적용”, 2013년 한국청정기술학회 춘계 학술발표회, 여수 경도리조트, 3. 28-29 (2013)
16. **윤양식**, 최영보, 윤다님, 박홍석, 이종협, “글리세롤의 산화탈수반응을 위한 다공성 산성 나노촉매의 제조 및 분석”, 한국화학공학회 봄 총회 및 학술대회, 제주국제컨벤션센터, 4.25-27 (2012)
17. 박대성, 곽병규, 김태용, 박재률, **윤양식**, 이종협, “다공성 구형 실리카에 담지된 헤테로폴리산 촉매의 제조 및 불균일 촉매반응에의 적용”, 추계 한국화학공학회, 송도컨벤시아, 10. 26-28 (2011)

18. 곽병규, 박대성, 박재률, **윤양식**, 김태용, 이종협, “폐글리세롤 수소첨가분해반응용 $CuCr_2O_4$ 촉매에서 조촉매의 효과”, 추계 한국화학공학회, 송도컨벤시아, 10. 26-28 (2011)